Ascent and emplacement dynamics of obsidian lavas inferred from microlite textures

- Authors
- Authors and affiliations

- Kenneth S. Befus
- Michael Manga
- James E. Gardner
- Matthew Williams
- o
- o
- o
- o

1. 1.
2. 2.

Research Article
First Online: 16 September 2015

Abstract

To assess the eruption and emplacement of volumetrically diverse rhyolite lavas, we measured microlite number densities and orientations from samples collected from nine lavas in Yellowstone Caldera and two from Mono Craters, USA. Microlite populations are composed of Fe-Ti oxides ± alkali feldspar ± clinopyroxene. Number densities range from $10^{8.11 \pm 0.03}$ to $10^{9.45 \pm 0.15}$ cm^{-3} and do not correlate with distance from the vent across individual flows and are remarkably similar between large- and small-volume lavas. Together, those observations suggest that number densities are unmodified during emplacement and that ascent rates in the conduit are similar between small domes and large lava flows. Microtextures produced by

continuous decompression experiments best replicate natural textures at decompression rates of 1–2 MPa hr^{-1}. Acicular microlites have a preferred orientation in all natural samples. Because the standard deviation of microlite orientation does not become better aligned with distance travelled, we conclude that microlites exit the conduit aligned and that strain during subaerial flow was insufficient to further align microlites. The orientations of microlite trend and plunge in near-vent samples indicate that pure shear was the dominant style of deformation in the conduit. We speculate that collapsing permeable foam(s) provides a mechanism to concurrently allow microlite formation and alignment in response to the combination of degassing and flattening by pure shear.

Keywords

Microlite Rhyolite Degassing Obsidian Yellowstone Mono craters

Editorial responsibility: P. Wallace

Electronic supplementary material

The online version of this article (doi: 10.1007/s00445-015-0971-6) contains supplementary material, which is available to authorized users.

Introduction

Rhyolite lavas span eruptive volumes up to 70 km^3, but such large-volume effusions have never been witnessed (Walker et al. 1973; Christiansen et al. 2007). The eruptive behavior and emplacement of large lavas have been instead inferred from textural and structural field studies of Holocene flows, in conjunction with direct observations of recent small-volume lavas (e.g., Fink 1980; 1983; Stevenson et al. 1994; Gregg et al. 1998; Iezzi and Ventura 2000; Castro et al. 2002; Smith 2002; Rust et al. 2003; Cañón-Tapia and Castro 2004; Pallister et al. 2013; Tuffen et al. 2013). One textural feature used for inferring the behavior of effusive eruptions is the orientation of elongated microlites, which are thought to act as rigid flow indicators and thus record lava deformation (Jeffery 1922; Manga 1998; Castro et al. 2002). Microlites are small (<100 μm) crystals that grow in response to undercooling, which results from degassing during ascent and cooling during emplacement.

Microlites have been used to infer the emplacement dynamics of Obsidian Dome (0.17 km^3) from Mono-Inyo Craters, USA (Miller 1985; Castro et al. 2002) and Douglas Knob (0.011 km^3) from Yellowstone Caldera, USA (Befus et al. 2014). Populations of microlites in both flows are aligned and generally trend in the flow direction inferred from topography and surface features. At Obsidian Dome, their orientations were found to progressively align in the flow with distance, possibly because the lava accumulated strain

during flow (Castro et al. 2002). In contrast, microlites do not become better aligned in Douglas Knob. Instead, their orientations are thought to record strain in the conduit, with little subsequent modification within the surface flow (Befus et al. 2014). It is possible that the discrepant conclusions between those studies may be attributed to sampling and baseline assumptions. For example, at Obsidian Dome, sampling occurred at the distal flow front and relied on a single sample from a drill core to infer near-vent orientations. Because microlites were near randomly oriented in the core sample, orientations were considered to be near random upon exiting the conduit and alignment observed in distal samples was caused by flow-induced strain. Conversely, at Douglas Knob, samples were collected systematically over the upper surface of the lava dome, with less control on microlite orientation in the conduit or at depth. But, the samples near the vent may show that significant orientation occurs just before lava extrudes the vent. Clearly, while there is potential to gain insights into how rhyolite lavas erupt using microlites, detailed microtextural studies have only been performed on two small-volume lavas.

Here, we present an extensive microtextural study of rhyolitic lavas that range in volume from 0.001 to 70 km^3 to investigate how microlite number densities and orientations vary with distance from the vent and eruptive volume. We constrain eruptive ascent rates by comparing natural microtextures with those generated in continuous decompression experiments. We find that microlite textures are similar across 5 orders of magnitude in erupted volume. Importantly, their assemblages, number densities, and orientations do not change with distance travelled in individual flows and are thus not modified during emplacement. Instead, textures preserve a record of conduit processes and may be used to gain new quantitative understanding of ascent and deformation in the conduit.

Samples and methods

Microlite textures were quantified in samples collected from lavas from the Central Plateau Member rhyolites from Yellowstone Caldera, WY and from Mono Craters, CA (Table 1). Each lava contains less than 10 % phenocrysts by volume in a matrix of high-silica rhyolite glass and abundant acicular microlites. Lavas were selected to encompass a range of flow thickness (17 to 200 m) and eruptive volume (0.001 to 70 km^3) (Table 1). Dense obsidian was collected from the targeted lava domes and flows from largely homogenous, in situ outcrops with 2 to 30 m^2exposure. We collected samples systematically across the lavas from near-vent positions to flow fronts. We define near-vent samples as those collected a few 10s to 100s of meters away from the vent, which in most cases represent only a small fraction of the total distance travelled by the lavas. Outcrops at both Yellowstone and Mono Craters rarely displayed pronounced, macroscopic flow banding, and when bands were present, they were planar. Some

samples contained sparse spherulites, which clearly overprint and postdate microlite textures. Microlite measurements were never performed within 10 mm of spherulites. Orientations of the samples were recorded in the field by measuring the strike and dip of one surface of the sample. Polished thin sections were prepared from those samples, with the field orientation recorded on each thin section.

Table 1

Physical characteristics of targeted lava flows and domes

		Age (ka)	Volume (km^3)	Max length (km)	Thickness (m)
Central Plateau Member lavas	Pitchstone Plateau (16)	79 ± 11	70	16.5	200
	Grants Pass (2)	72 ± 3	0.5	2.4	37
	Solfatara Plateau (15)	103 ± 8	7	15.30	57
	West Yellowstone (25)	114 ± 1	41	21.70	105
	Trischmann Knob (2)	~115	0.014	0.25	17
	Douglas Knob (11)	~115	0.011	0.13	70
	Bechler River (2)	116 ± 2	8	13.70	35
	Summit Lake (11)	124 ± 10	37	17.70	92
	Buffalo Lake (1)	160 ± 3	54	16	97
	Dry Creek (1)	166 ± 9	9	10	53
Mono Craters lavas	South Dome (6)	0.66 ± 0.02	0.001	0.08	30
	Northwest	1.5 ± 0.3	0.3	1	150

	Age (ka)	Volume (km^3)	Max length (km)	Thickness (m)
Coulee (10)				

Data is compiled from Sieh and Bursik (1986), Wood (1983), Christiansen (2001), Christiansen et al. (2007), and Befus et al. (2014). Number of samples are shown in parentheses after flow name

At Yellowstone, we collected 1–2 kg samples of dense obsidian from nine lava flows: Pitchstone Plateau, Grants Pass, Solfatara Plateau, West Yellowstone, Trischmann Knob, Bechler River, Summit Lake, Buffalo Lake, and Dry Creek (Fig. 1). All are part of the Central Plateau Member, which consists of ~30 obsidian lava flows and domes that erupted within Yellowstone Caldera between 79 to 166 ka (Christiansen et al. 2007). All units are compositionally similar, comprised of 5–10 vol% phenocrysts of quartz, sanidine ($Or_{50\pm2}Ab_{47\pm2}$), magnetite ($Mgt_{48\pm2}$), fayalite ($Fa_{94\pm2}$), and clinopyroxene ($En_{13\pm2}$) all set in a high-silica rhyolitic (76.5 ± 1.0 wt% SiO_2) glassy matrix. Prior to eruption the magmas were stored at 750 ± 25 °C and 50 to 150 MPa in the shallow crust (Fig. 2) (Befus et al. 2014; Befus 2014).

Open image in new window

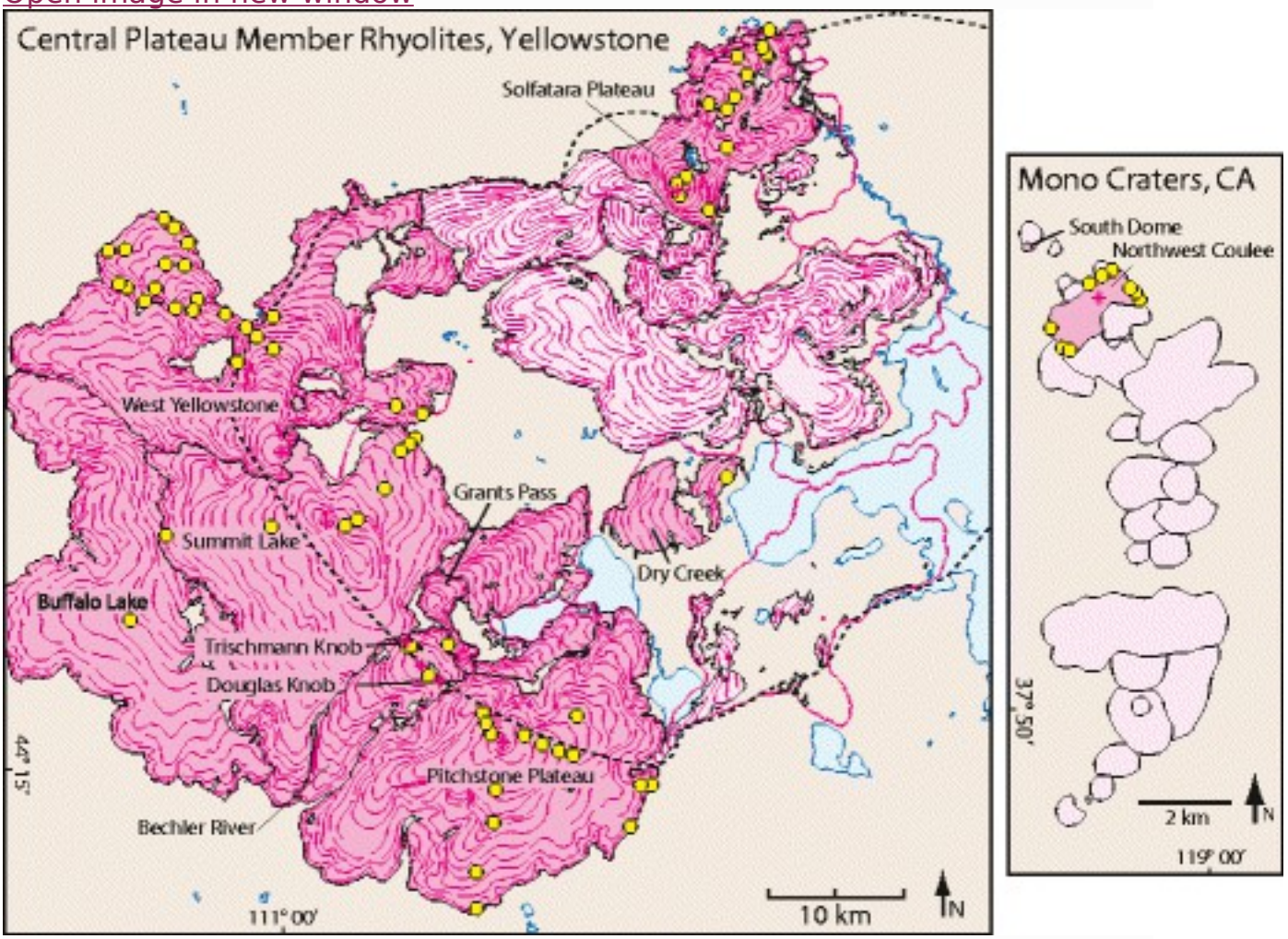

Fig. 1

Simplified geologic maps of Central Plateau Member rhyolites in the Yellowstone Caldera, WY and Mono Craters, CA modified after Christiansen (2001) and Sieh and Bursik (1986). Lava flows are shown in *pink*, with sampled lavas labeled in a *darker shade. Dark pink lines* on Central Plateau Member lavas represent pressure ridges. *Small pink stars* show approximate vent locations. The extent of Yellowstone Caldera is shown by the *dashed black line*. Sample locations are shown by *yellow circles*, except on South Dome of Panum Crater because of overcrowding

Open image in new window

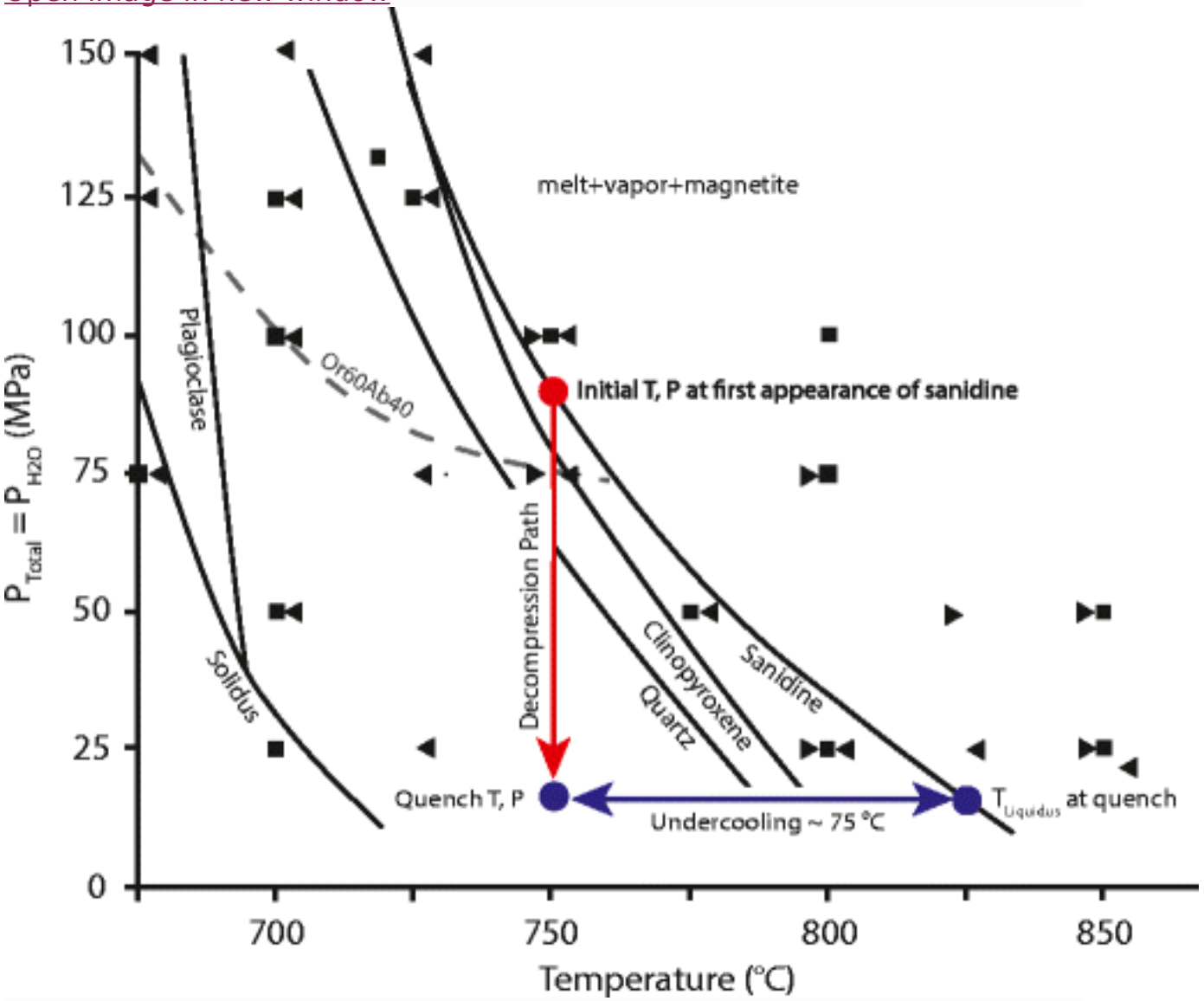

Fig. 2
Phase equilibria diagram assuming $P_{total} = P_{H2O}$ (modified after Befus 2014). *Squares*are initial experiments using powder from sample Y82, whereas *right and left pointing triangles* represent melting and crystallization experiments, respectively. *Lines* represent mineral stability curves. The *dashed gray line* marks a contour for sanidine composition. A decompression experiment (*red arrow*) at 750 °C is used to demonstrate the concept of undercooling (Δ*T*, *blue arrow*), which is equal the difference between the sanidine in curve and the experiment at the quench pressure

Pitchstone Plateau and Summit Lake flows represent large-volume rhyolites (70 and 37 km^3, respectively) that extruded from fissure vents. Samples from those flows were collected along transects that extended from near vent to flow front. Similarly, we collected samples across the length of

Solfatara Plateau, an elongate 7-km^3 lava that travelled up to 16 km. We focused on the northwestern lobe of West Yellowstone lava flow where the lava broke through a breach in the caldera wall and was subsequently emplaced through that restriction ("chute") and over a relatively flat plain. The chute is located 9 km from the vent (Christiansen 2001). Today, the western lobe of West Yellowstone is preserved as a lobate body that extends ~11 km beyond the chute. This lobe presents an ideal case to examine how microtextures vary when emplacement happens independent of conduit forcing. We collected samples systematically across the length and breadth of the western lobe, as well as in the ponded domain up to 3 km upstream from the chute. Finally, we present microtextural data from samples collected from Grants Pass, Trischmann Knob, Bechler River, Buffalo Lake, and Dry Creek lavas and include results from Douglas Knob discussed originally in Befus et al. (2014).

At Mono Craters, we collected 1–2 kg samples from Northwest Coulee and the South Dome of Panum Crater (Fig. 1). Mono Craters is a volcanic chain comprised of 27 rhyolitic domes, flows, and associated pyroclastic deposits that erupted ~660 to 20,000 years ago along a gentle arcuate trend between Mono Lake and Long Valley Caldera (Wood 1983; Sieh and Bursik 1986; Hildreth 2004). Northwest Coulee is a ~0.3-km^3 lava that erupted 1500 ± 300 years ago from a central fissure (Wood 1983). Panum Dome is a composite of four domes that were emplaced 660 ± 20 years ago within the Panum Crater tephra ring (Sieh and Bursik 1986). We sampled surface outcrops of dense obsidian only from the 0.001 km^3 South Dome at Panum Crater, an obsidian dome emplaced via exogenous growth symmetrically about a central fissure (Sieh and Bursik 1986). Importantly, South Dome presents a volumetric end member in which lava experienced negligible transport away from the conduit (<100 m). Northwest Coulee and Panum Dome belong, respectively, to the sparsely porphyritic and aphyric classifications assigned by Kelleher and Cameron (1990). They contain sparse (0–3 vol%) phenocrysts of quartz, plagioclase ($Ab_{77 \pm 3}$), sanidine ($Or_{65 \pm 4}$), fayalite ($Fa_{\sim 93}$), Fe-rich hornblende, Ti-rich biotite, orthopyroxene, magnetite, and ilmenite (Williams et al. 2012). Most minerals fail compositional equilibrium tests (e.g., Bacon and Hirschmann 1988), and so the pre-eruptive temperature and pressure conditions of Mono Craters magmas are undefined.

Microlite characterizations

Microlite number density (MND) was measured by counting all microlites in rectangular prismatic sub-volumes of thin sections while continuously focusing through the transparent glass using a petrographic microscope (Table 2). Rectangular volumes were generally 80 µm wide, 80 µm long, and 30 µm deep. Depth was measured using a linear encoder attached to the focusing drive of the petrographic microscope. We counted microlites at

multiple positions across each sample to compile a statistically significant number of microlites. Number density counts include separate tallies for Fe-Ti oxide, clinopyroxene, and alkali feldspar microlites, with total MND representing the sum of all phases. Each phase occurs as euhedral crystals in the glassy groundmass (Fig. 3). Overall, the MND dataset is based upon individually characterizing and logging 59,500 microlites in natural samples and experiments.

Table 2

Microlite number density and microlite orientations

	Sample	UTM coordinates	Total (log # cm^{-3})	Oxide (log # cm^{-3})	Pyroxene (log # cm^{-3})	Feldspar (log # cm^{-3})
Pitchstone Plateau	Average		9.01 ± 0.39	8.84 ± 0.31	8.25 ± 0.85	1.08 ± 2.86
$n = 5420$ (MND)	Yell 15	527747/4899455	9.26–9.45	8.89–9.02	9.02–9.25	0
$n = 1320$ (Orient)	Yell 20	518029/4902499	8.90–8.99	8.86–8.89	7.91–8.25	0
	Yell 21	518540/4902023	8.50–8.87	8.40–8.80	6.75–8.02	0
	Yell 22	519894/4900303	9.08–9.14	9.01–9.11	7.94–8.25	0
	Yell 23	521796/4899169	8.30–8.50	7.93–8.48	0–7.30	0–8.05
	Yell 25	514414/4889716	9.37–9.54	9.17–9.34	8.93–9.10	0
	Y112	515961/4902434	–		–	–
	Y113	516140/4903494	–	–	–	–
	Y114	515999/4904434	–	–	–	–
	Y149	528043/4899265	9.21–9.27	8.82–8.97	8.97–8.98	0

	Sample	UTM coordinates	Total (log # cm^{-3})	Oxide (log # cm^{-3})	Pyroxene (log # cm^{-3})	Feldspar (log # cm^{-3})
	Y150	525977/4895300	–	–	–	–
	Y185	517178/4897717	–	–	–	–
	Y186	515902/4895582	–	–	–	–
	Y187	515071/4891401	–	–	–	–
	Y188	514413/4889707	–	–	–	–
	Y193	523241/4901708	–	–	–	–
Solfatara Plateau	Average		8.94 ± 0.40	8.82 ± 0.45	6.25 ± 3.62	0.99 ± 2.43
$n = 6009$ (MND)	Y46	533836/4950365	9.28–9.33	9.22–9.23	8.29–8.61	0
$n = 264$ (Orient)	Y50	533139/4949057	8.26–8.68	8.24–8.66	0–6.99	0
	Y60	536520/4953333	8.66–8.69	8.56–8.59	9.98	0
	Y76	531805/4941733	9.20	9.13	8.37	0
	Y77	531604/4945591	9.38	9.38	0.00	0
	Y81	530296/4944052	9.19	9.06	8.60	0
	Y84	529639/4942656	8.52	8.41	7.86	0

	Sample	UTM coordinates	Total (log # cm^{-3})	Oxide (log # cm^{-3})	Pyroxene (log # cm^{-3})	Feldspar (log # cm^{-3})
	Y87	529880/4942010	9.26	9.26	7.30	0
	Y129	533967/4942410	8.10–8.22	8.09–8.21	0.00	0
	Y134	536407/4955119	8.47–8.64	7.94–8.21	8.32–8.44	0
	Y138	536150/4953789	8.93–9.00	8.36–8.55	8.77–8.83	0–6.99
	Y143	535794/4951685	9.16	9.15–9.16	0.00	0
	Y144	531944/4950111	9.21–9.51	8.93–8.59	8.84–8.95	0–6.94
	Y223	533447/4947138	–	–	–	–
	Y241	529759/4943340	–	–	–	–
Summit Lake	Average		8.98 ± 0.31	8.71 ± 0.39	8.00 ± 0.74	4.08 ± 4.48
$n = 4992$ (MND)	Yell 54	507391/4921840	8.59–9.47	8.29–9.21	8.27–9.11	0.00
$n = 660$ (Orient)	Yell 56	508053/4923253	8.61–9.15	8.50–8.59	7.14–7.95	6.96–9.03
	Yell 57	509321/4924062	7.85–8.59	7.78–8.23	0–7.66	0–8.9
	Yell 58	509553/4924796	9.20	9.17–9.18	7.11–7.30	7.51–7.74
	Y71	506033/4918669	9.13–9.43	8.56–8.91	8.99–9.28	0.00

	Sample	UTM coordinates	Total (log # cm^{-3})	Oxide (log # cm^{-3})	Pyroxene (log # cm^{-3})	Feldspar (log # cm^{-3})
	Y72	505270/4917940	8.93–9.44	8.87–9.20	8.03–8.12	0.00
	Y195	492222/4915841	–	–	–	–
	Y198	501561/4917443	–	–	–	–
	Y199	505988/4918910	–	–	–	–
	Y201	507420/4921681	–	–	–	–
	Y202	508436/4923560	–	–	–	–
West Yellowstone $n = 3491$ (MND) $n = 2244$ (Orient)	Average		9.45 ± 0.15	9.37 ± 0.13	8.68 ± 0.24	4.70 ± 4.08
	Yell 6	510511/4925929	9.38–9.70	9.31–9.59	7.82–8.48	0–7.60
	Yell 16	510154/4925898	9.05–9.56	8.99–9.49	7.07–8.17	0–6.89
	Yell 17	508615/4926453	9.38–9.59	9.28–9.51	8.27–8.70	0
	Y161	492121/4935069	–	–	–	–
	Y162	496300/4933345	–	–	–	–
	Y165	490411/4934556	–	–	–	–
	Y166	489201/4935453	–	–	–	–

	Sample	UTM coordinates	Total (log # cm^{-3})	Oxide (log # cm^{-3})	Pyroxene (log # cm^{-3})	Feldspar (log # cm^{-3})
	Y167	488443/4935747	–	–	–	–
	Y169	488961/4936836	–	–	–	–
	Y171	494070/4933833	–	–	–	–
	Y172	493717/4934611	–	–	–	–
	Y175	491159/4937315	–	–	–	–
	Y176	490650/4935523	–	–	–	–
	Y183	491762/4940196	–	–	–	–
	Y184	491768/4940838	–	–	–	–
	Y190	487705/4938221	–	–	–	–
	Y191	488516/4938568	–	–	–	–
	Y205	492517/4937176	–	–	–	–
	Y207	492881/4938379	–	–	–	–
	Y209	492874/4934227	–	–	–	–
	Y210	497431/4932832	–	–	–	–

	Sample	UTM coordinates	Total (log # cm^{-3})	Oxide (log # cm^{-3})	Pyroxene (log # cm^{-3})	Feldspar (log # cm^{-3})
	Y211	498555/4932257	–	–	–	–
	Y213	498913/4932199	–	–	–	–
	Y215	497664/4930953	–	–	–	–
	Y217	500000/4931296	–	–	–	–
Grants Pass	Average		8.79 ± 0.72	8.71 ± 0.39	8.02 ± 0.69	0
n = 784 (MND)	Y101	512762/4909368	9.00–9.43	8.85–9.39	8.39–8.62	0
	Y102	513081/4910457	8.21–8.39	8.14–8.29	7.39–7.72	0
Trischmann Knob	Average		8.11 ± 0.03	8.00 ± 0.17	7.01 ± 0.93	0
n = 864 (MND)	Y96	509861/4909406	7.61–8.36	7.45–8.13	7.12–7.96	0
	Y97	510036/4909483	7.95–8.21	7.91–8.21	0–6.84	0
Bechler River	Average		8.63 ± 0.49	8.30 ± 0.54	8.35 ± 0.45	3.01 ± 4.26
n = 1079 (MND)	Y98	511802/4909501	8.26–8.32	7.87–7.94	7.96–8.13	5.97–6.27
	Y99	512034/4907275	8.94–9.01	8.64–8.77	8.63–8.71	0
Buffalo Lake *n* = 1191	Yell 65	487232/4905800	9.04	9.04	0	0

	Sample	UTM coordinates	Total (log # cm^{-3})	Oxide (log # cm^{-3})	Pyroxene (log # cm^{-3})	Feldspar (log # cm^{-3})
(MND)						
Dry Creek $n =$ 451 (MND)	Yell 40	534704/4922057	8.58	8.52	7.73	0
Douglas Knob[b]	Average		8.40 ± 0.43	8.28 ± 0.48	7.20 ± 0.49	3.09 ± 3.89
$n = 9564$ (MND)	Y88	512231/4906940	7.59–8.21	7.53–8.18	0–7.35	0–7.13
$n = 1682$ (Orient)	Y89	512265/4906785	8.70–9.60	8.70–9.58	0–8.29	0
	Y90	512265/4906688	7.57–8.39	7.57–8.34	0–7.73	0
	Y92	512078/4906606	8.27–8.72	7.70–8.52	0–8.11	7.97–8.52
	Y116	512648/4906531	8.29–8.91	8.29–8.86	0–7.90	0
	Y117	512170/4906575	7.57–8.83	7.52–8.83	0–6.89	0
	Y118	512004/4906729	7.37–8.63	7.25–8.41	0–8.14	0–7.77
	Y119	512038/4906903	7.60–8.79	8.55–8.79	0–7.36	0
	Y120	412268/4906783	8.00–9.08	7.98–9.08	0–7.74	0
	Y121	512344/4906703	8.04–8.71	8.00–8.71	0–7.34	0–7.88
	Y122	512222/4906940	8.09–9.17	8.08–8.98	0–8.71	0

	Sample	UTM coordinates	Total (log # cm^{-3})	Oxide (log # cm^{-3})	Pyroxene (log # cm^{-3})	Feldspar (log # cm^{-3})
Northwest Coulee	Average		9.26 ± 0.38	8.34 ± 0.50	9.19 ± 0.37	5.07 ± 3.16
$n = 9128$ (MND)	NWC-2	321241/4197301	8.92–9.37	7.65–8.19	8.90–9.35	0
$n = 2178$ (Orient)	NWC-3a	321360/4197315	9.42–9.50	8.17–8.77	9.36–9.45	0
	NWC-3b	21360/4197316	–	–	–	–
	NWC-4	322570/4198386	9.01–9.66	7.22–8.85	8.92–9.59	0–7.41
	NWC-5	322437/4198490	8.36–9.47	7.57–8.54	8.25–9.42	0–7.76
	NWC-6	322417/4198540	9.94–10.20	9.22–9.63	9.85–10.07	0–7.41
	NWC-7	321445/4198672	8.74–9.52	7.57–8.74	8.70–9.4	0–7.25
	NWC-8	322013/4199084	7.56–10.10	7.02–9.25	7.37–10.03	0–7.33
	NWC-9a	321777/4198896	7.69–10.11	6.37–9.47	7.67–9.99	0–6.97
	NWC-21	320868/4197489	–	–	–	–
South Dome	Average		8.46 ± 0.75	7.92 ± 0.56	7.95 ± 0.63	2.35 ± 4.05
$n = 2428$ (MND)	PCD-3	320230/4199804	7.11–8.97	6.86–8.26	6.39–8.87	0–6.69
$n = 792$ (Orient)	PCD-6	320242/4199697	9.66–9.11	8.70–8.97	8.58–9.07	9.53–9.83

	Sample	UTM coordinates	Total (log # cm^{-3})	Oxide (log # cm^{-3})	Pyroxene (log # cm^{-3})	Feldspar (log # cm^{-3})
	PCD-7	320102/4199682	7.03–9.24	6.93–9.14	6.33–9.23	0
	PCD-8	320134/4199673	7.43–9.10	6.98–8.56	7.24–8.95	0
	PCD-10	320164/4199664	7.32–9.86	7.14–9.23	6.43–8.34	0–9.73
	PCD-12	320137/4199741	7.28–7.80	6.92–7.57	6.70–7.67	0

Dashed fields (−) microlite texture was not quantified

[a]Aspect ratio is the ratio of length to width of the population of acicular microlites used in orientation dataset. Values in parentheses are the standard deviation

[b]Data for Douglas Knob is from Befus et al. (2014)

Open image in new window

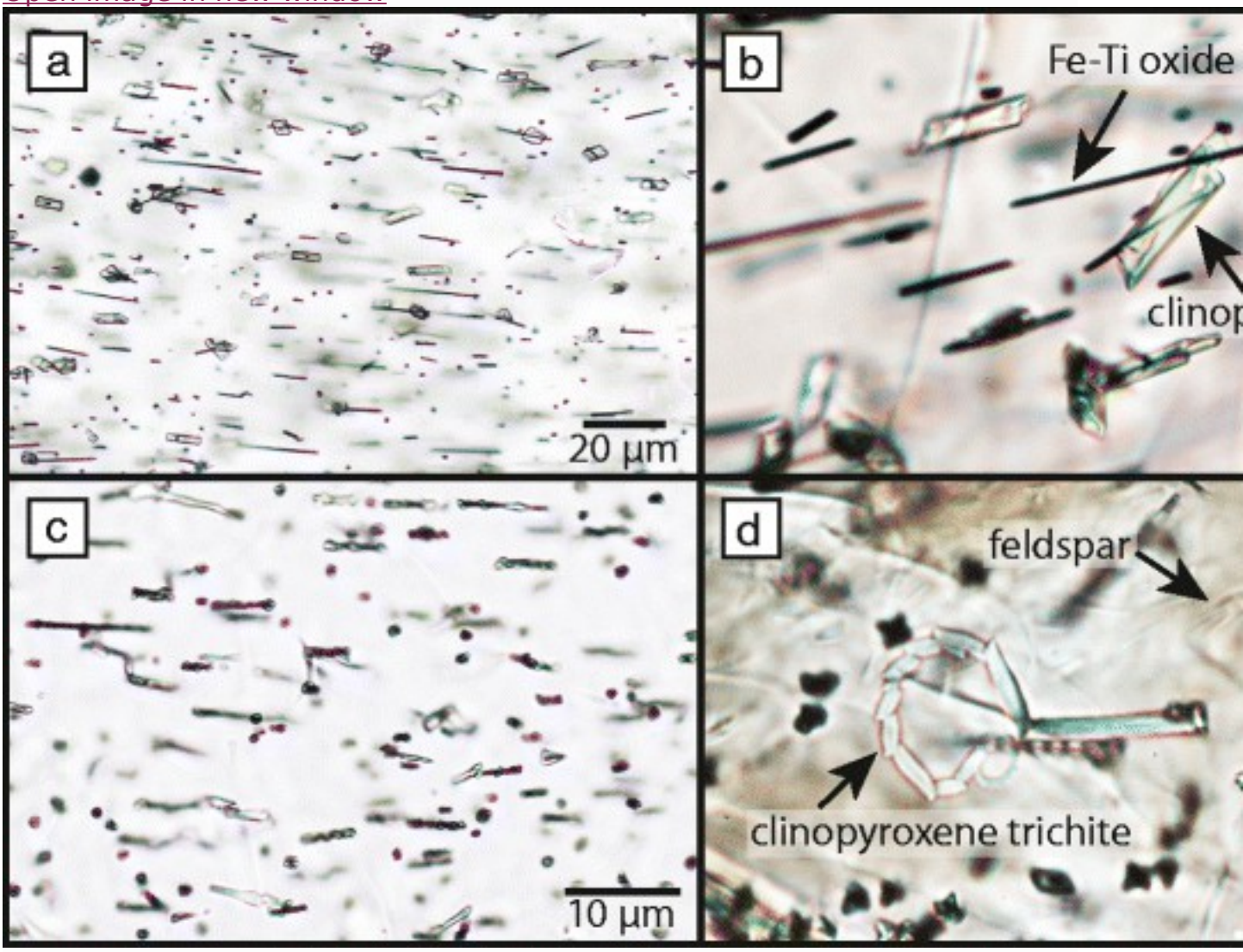

Fig. 3
Representative photomicrographs of microlites. **a** Moderate MND groundmass with preferentially aligned Fe-Ti oxides (*black acicular*), some with clinopyroxene overgrowths (*clear prisms*). **b** Fe-Ti oxides and clinopyroxene crystals. **c** Preferentially aligned Fe-Ti oxide microlites encrusted with clinopyroxene overgrowths. **d** A clinopyroxene trichite that cuts across primary fabric containing Fe-Ti oxides with clinopyroxene overgrowths and feldspar laths (similar index of refraction to glass makes them difficult to see)

Some samples are banded, with bands defined by differences in MND and mineral assemblages. In those, we measured MND separately for the high and low MND domains. Trichites and globulites—microlites with delicate and unusual curved morphologies—comprised of Fe-Ti oxide and clinopyroxene were observed in some samples (Fig. 3). Because such fragile crystals are unlikely to be preserved in an actively deforming fluid, they most likely

represent post-emplacement crystallization (Harker 1897; Davis and McPhie 1996). We consequently did not count them with the other microlites.

Microlite orientations were measured petrographically, following the methodology described in Befus et al. (2014) with a procedure adapted from Castro et al. (2003). Briefly, we measured the trend (ϕ) of an acicular microlite using the stage goniometer, whereas its length and width were measured using the eyepiece reticle. Next, we measured the depth in the thin section to each microlite tip by focusing through the transparent obsidian and recording the depth measured by the linear encoder. Together, those measurements were used to calculate the true length and plunge (θ) of each microlite. Trend and plunge measurements are accurate to ±0.5° and ±2°, respectively. The orientations of at least 140 microlites were measured in each sample. To maintain consistency, we only measured acicular microlites with aspect ratios between 6:1 and 14:1 (Table 2). Microlite orientations were then rotated to their true field orientation using *Stereonet* (Cardozo and Allmendinger 2013). In all, the orientation dataset consists of >13,500 measurements. The average ϕ and θ of each population was calculated, with the degree of alignment for each population measured by the standard deviation of ϕ and θ (σ_{φ} and σ_{θ}), with smaller standard deviations indicating better alignment (Table 2) (Manga 1998).

Experimental techniques

A portion of sample Y82 from Solfatara Plateau, crushed to a ~50-μm powder, was used as starting material for experiments. Sample Y82 is compositionally representative of Central Plateau Member rhyolites and contains 5–10 % phenocrysts of quartz, sanidine, clinopyroxene, fayalite, and magnetite, all hosted in a glassy high-silica rhyolite matrix (77 ± 2 wt% SiO_2) (Table 3). In each experiment, enough water was added to the capsules to ensure water saturation at the experimental temperature and pressure conditions. The first step in running decompression experiments is to synthesize melts in equilibrium with expected pre-eruptive magmatic conditions. To this end, we performed a set of phase equilibria experiments (Table 4). Experiments were performed following the methods described in Befus (2014). Experiments were prepared by partially filling $Ag_{70}Pd_{30}$ capsules that were welded shut at one end with powder from Y82 and enough distilled water to ensure saturation. Next, the open end of the capsules was welded shut. The sealed capsules were loaded with filler rods into cold-seal pressure vessels, which in turn were inserted in furnaces. Pressure was controlled by a hydraulic pressure system, whereas oxygen fugacity was maintained by mixed buffer powder and/or the composition of the filler rods (Ni for NNO + 1 and steel for QFM). After ~5 days, each experiment was quenched in 1 to 2 min by blowing on the pressure vessel with compressed air and then submerging it in water. A small portion of each sample was

prepared for petrographic analysis, and the remainder was crushed into a fine powder to be used as starting material for decompression experiments.

Table 3

Compositions of matrix glass and major phenocryst phases in sample Y82 used as starting material in experiments

Phase	SiO_2	TiO_2	Al_2O_3	FeO[a]	MgO	MnO	CaO	K_2O	Na
Matrix glass	76.85 (1.84)	0.12 (0.06)	12.06 (0.22)	1.57 (0.25)	0.02 (0.02)	0.09 (0.06)	0.47 (0.04)	5.12 (0.19)	4.((0.)
Fayalite	30.09 (0.33)	0.04 (0.05)	0.01 (0.01)	64.88 (0.91)	2.75 (0.10)	1.62 (0.08)	0.28 (0.01)	–	–
Clinopyroxene	49.45 (0.76)	0.21 (0.08)	0.45 (0.15)	26.70 (0.61)	4.12 (0.39)	0.73 (0.05)	18.68 (0.24)	–	0. (0.)
Magnetite	0.09 (0.03)	18.53 (0.65)	0.85 (0.08)	76.39 (1.12)	0.18 (0.03)	0.87 (0.04)	0.01 (0.01)	–	–
Sanidine	66.42 (0.59)	–	18.94 (0.22)	0.09 (0.07)	–	–	0.39 (0.18)	8.28 (0.61)	5.5 (0.)

Analyses by electron microprobe. Major oxides are reported in weight percent and are averages of *n* samples. Values in parentheses represent standard deviations

"–" oxide was not analyzed

[a]Total iron reported as FeO

Table 4

Experimental conditions, mineralogy, and textures of experiments used as starting materials for decompression experiments

	Experiment	*P* (MPa)	*T* (°C)	Duration (h)	fO_2	Stable phases[b]	log total MND	log feld MND
Starting materi	23	75	750	118	NNO + 1	gl, mgt, feld	9.6 ± 0.1	8.2 ± 0.2

	Experiment	*P* (MPa)	*T* (°C)	Duration (h)	*f* O_2	Stable phases[b]	log total MND	log feld MND
als[a]	51	50	780	100	NNO + 1	gl, mgt, rare pyx, and feld	9.5 ± 0.5	0 to 8.0 ± 0.3
	53	50	780	122	NNO + 1	gl, mgt, pyx, feld	10.0 ± 0.7	0 to 8.0 ± 1.0
	57	130	720	120	NNO + 1	gl, mgt, pyx, feld	10.6 ± 0.1	9.3 ± 0.1
	58	90	780	120	NNO + 1	gl, mgt	10.0 ± 0.7	0
	72	100	800	120	NNO + 1	gl, mgt	10.2 ± 0.2	0
	96	100	750	116	QFM	gl, pyx, feld, fay	10.2 ± 0.2	8.5 ± 0.3
	106	100	750	120	QFM	gl, pyx, feld, fay	9.6 ± 0.1	7.8 ± 0.2
	120	100	775	120	NNO + 1	gl, mgt	10.0 ± 0.4	0
	121	100	775	120	QFM	gl, mgt, rare pyx	10.6 ± 0.3	0

[a]Starting material is the powdered obsidian glass Y82 collected from Solfatara Plateau

[b]Stable phases are glass (gl), magnetite (mgt), clinopyroxene (pyx), fayalite (fay), and alkali feldspar (feld)

We performed three sets of isothermal decompression experiments, at 720, 750, and 780 °C, respectively (Table 5). Decompressions were performed in rapid-quench, Ni-alloy pressure vessel assemblages as described in Carroll and Blank (1997). Capsules for decompression experiments were prepared as described previously for phase equilibria experiments. To release pressure, we used a motorized stem valve, modified from that described in Nowak et al. (2011). In our modification, a *Eurotherm* process controller receives an electronic signal from the pressure gauge and sends voltages to a piezo stack ceramic motor in order to open and shut the stem valve. The amount of voltage sent to the motor controls the precise position of the needle. As the needle moves to the open position, pressure drops as water leaks from the system. The motor controls the decompression rate by switching from the closed to open positions at millisecond timescales. Decompressions are thus automated, and the system is responsive to pressure variations of less than 0.1 MPa.

Table 5

Experimental conditions, products, and textures in decompression experiments

	Experiment	Starting material[a]	P_i(MPa)	ΔT_i(°C)	P_f(MPa)	ΔT_f(°C)	Duration (h)	dP/ (MPa h^{-1})
720 °C	73	57	130	10	10	120	6	20.
	74	57	130	10	108	22	4.5	4.9
	79	57	130	10	10	120	24	5.0
	90	23	75	45	10	120	72	0.9
	91	23	75	45	30	90	50	0.9
	104	96	75	70	10	110	24	2.7

	Experiment	Starting material[a]	P_i(MPa)	ΔT_i(°C)	P_f(MPa)	ΔT_f(°C)	Duration (h)	dP/dt (MPa·h^{-1})
	107	106	130	37	10	110	72	1.7
750 °C	82	72	100	0	10	90	24	3.8
	83	72	100	0	30	55	18	3.8
	84	72	100	0	50	33	13	3.8
	86	23	75	10	10	90	72	0.9
	87	23	75	10	30	55	50	0.9
	93	23	75	10	10	90	24	2.7
	94	23	75	10	30	55	16.7	2.7
	95	51	75	10	10	90	24	2.7
	124	121	87	30	10	76	46.5	1.7
	125	121	87	30	39	60	25.3	1.9

	Experiment	Starting material[a]	P_i (MPa)	ΔT_i (°C)	P_f (MPa)	ΔT_f (°C)	Duration (h)	dP/dt (MPa h^{-1})
	127	121	87	0	34	52	45.5	1.2
	128	121	87	30	50	53	48	0.8
	129	120	87	0	50	33	48	0.8
	130	120	87	0	65	20	26.5	0.8
780 °C	55	53	50	3	5	63	60	0.8
	56	53	50	33	5	63	30	1.5
	60	58	90	0	10	56	6	13.
	69	58	90	0	10	56	24	3.3
	70	58	90	0	10	56	45	1.8
	105	96	75	8	10	44	24	2.7
	131	120	60	17	10	44	120	0.4

[a]Starting materials are powders of crushed material from previously run experiments (listed in Table 4)

[b]Crystals that formed during decompression experiments when compared to starting materials. Phases are quartz (qtz), clinopyroxene (pyx), fayalite (fay), and alkali feldspar (feld)

Decompression experiments began after initially annealing the sample at the starting pressure and temperature for 20 min. Starting materials for the

decompression experiments were run at temperature and pressure conditions near the liquidus (Fig. 2) (Befus 2014), thus the melts were initially undercooled (ΔT) by ~0 °C and had sparse microlites. Depressurization was then controlled by the automated continuous decompression system, with experiments lasting 4.5 to 120 h. Upon reaching final pressure, samples were quenched rapidly (≤5 s) by using a magnet to pull the sample out of the furnace and into the water-cooled jacket of the pressure vessel assemblage. In most experiments, samples were quenched at final pressures of 5 to 10 MPa in an attempt to suppress extensive bubble formation, which obscures microlite textures. At those pressures, the melts at 720, 750, and 780 °C are undercooled by approximately 120, 90, and 60 °C, respectively. Other experiments were quenched at higher pressures to track progressive crystallization along decompression pathways. After the pressure vessel cooled, the capsule was removed and checked for leaks. Last, the sample was removed, mounted in epoxy, and prepared for petrographic and microprobe analysis. Both starting materials and products of decompression experiments were characterized by identifying new crystallization, and MND was quantified for experiments run at 750 °C (Tables 4 and 5).

Results

Microlite textures in natural samples vary from being homogenous to being discretely to diffusely band in different microlite assemblages and number densities. Fe-Ti oxides are generally the most abundant, with lesser amounts of clinopyroxene and alkali feldspar, except in Northwest Coulee and South Dome, in which clinopyroxene predominates. Fe-Ti oxides, which are commonly overgrown by clinopyroxene, occur as equidimensional crystals, 1 to 2 µm in size, or as acicular rods 1 to 2 µm wide and 3 to 30 µm long. Clinopyroxene is present in all flows, except Buffalo Lake, and occurs as either individual crystals or as overgrowths on Fe-Ti oxides. Both types occur as skeletal to euhedral prismatic crystals, 1 to 10 µm wide and 2 to 20 µm long. Overgrowths tend to be more abundant and larger than free crystals. Alkali feldspar microlites occur in both lavas from Mono Craters and in six of the Central Plateau Member rhyolites. Alkali feldspar microlites occur as elongate laths, 1 to 5 µm wide and 2 to 20 µm long, and commonly have swallowtail terminations. Hopper and skeletal forms (Lofgren 1974) were not observed.

Total MND of individual flows ranges up to $10^{10.20}$ cm^{-3} but average from $10^{8.11 \pm 0.03}$ to $10^{9.45 \pm 0.15}$ cm^{-3} (Fig. 4). Fe-Ti oxide numbers average from $10^{7.92 \pm 0.56}$ to $10^{9.37 \pm 0.13}$ cm^{-3} (Fig. 5). Clinopyroxene and feldspar MND vary highly across flows, including being absent (Fig. 5). In fact, both are entirely absent in Buffalo Lake. When present, clinopyroxene MND ranges up to $10^{10.07}$ cm^{-3} and

feldspar ranges up to $10^{9.83}$ cm^{-3}. Number densities do not correlate between the phases.

Open image in new window

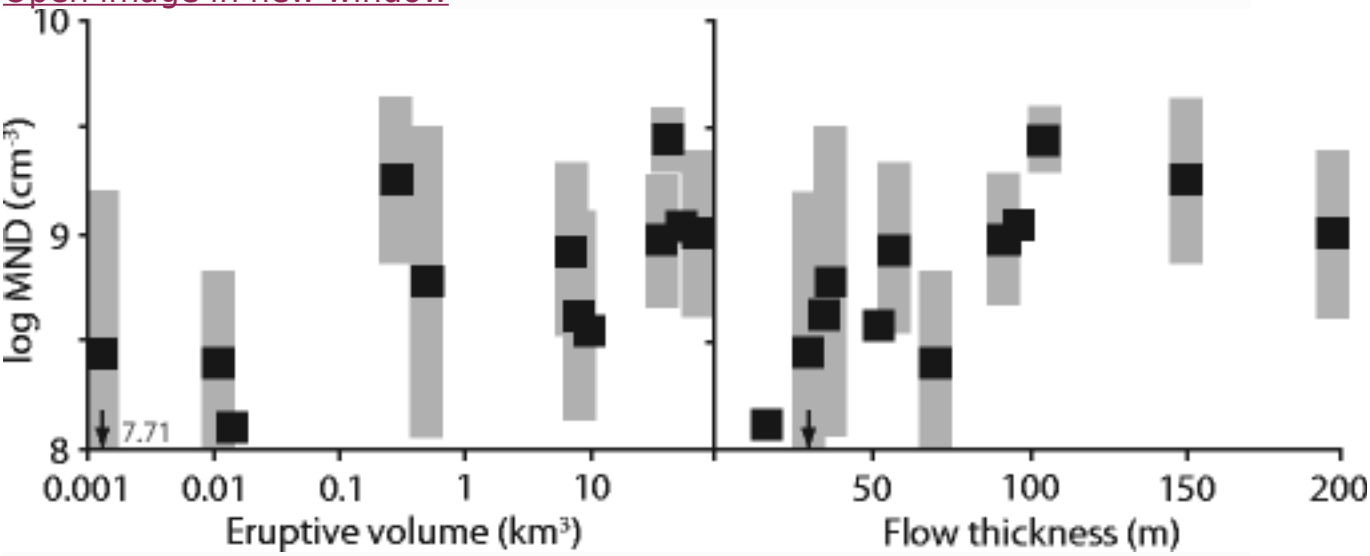

Fig. 4

Total MND (cm^{-3}) as a function of eruptive volume and flow thickness. *Black squares*represent average MND, whereas *gray bars* encompass full range. The samples with *downward pointing arrows* indicate log MND in that sample extends to values as low as 7.71 cm^{-3}

Open image in new window

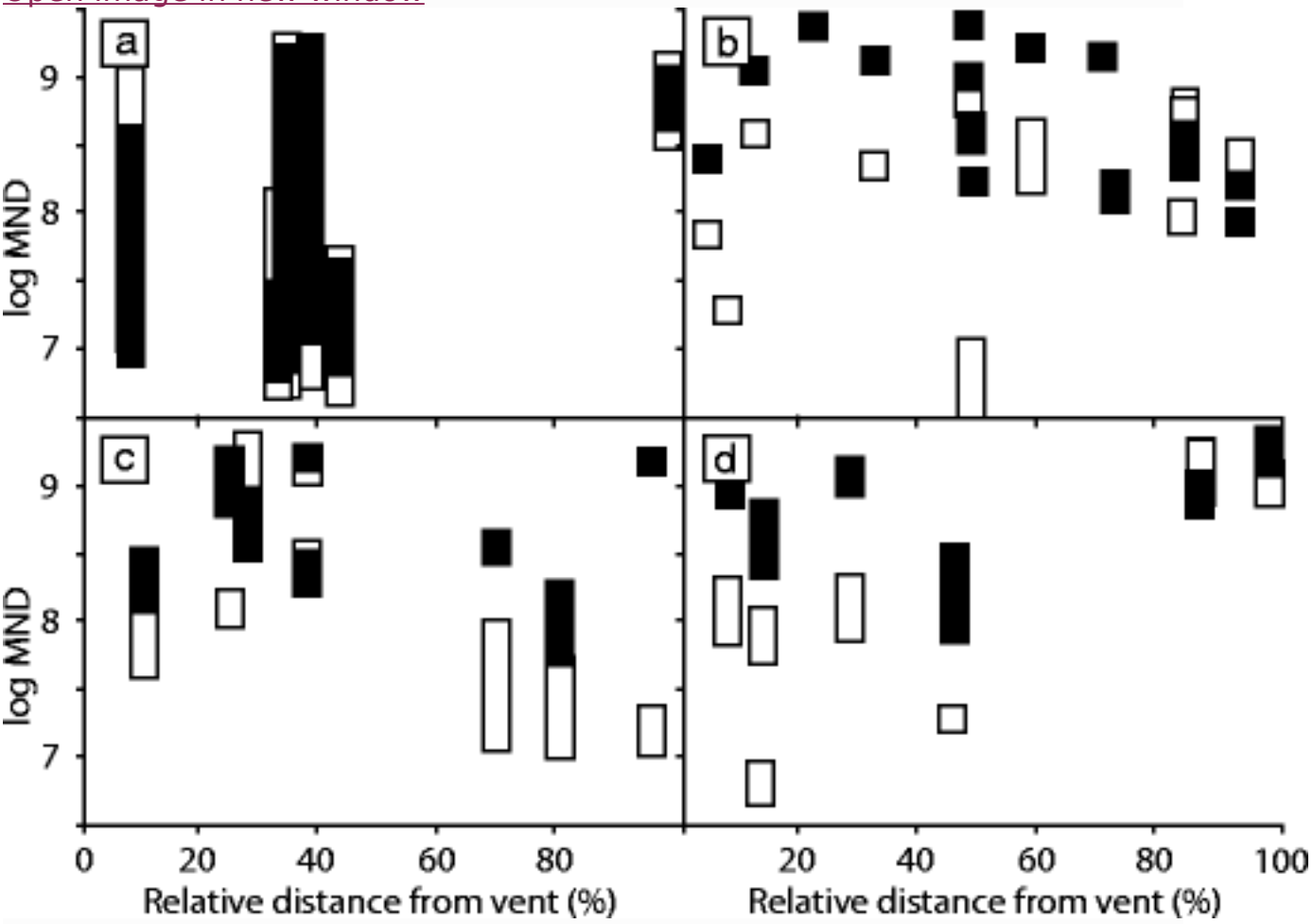

Fig. 5
MND as a function of relative position in **a** South Dome, **b** Solfatara Plateau, **c** Summit Lake, and **d** Pitchstone Plateau lavas. Relative distance from vent measurements are percentages of flow distance relative to maximum flow distance. *Black and white symbols* are for Fe-Ti oxides and clinopyroxene, respectively. The *vertical length of the symbol* represents the range of values in a single sample

Acicular microlites are preferentially aligned in samples from all flows (Fig. 6). Microlite plunge distributions are consistently more aligned than trend (e.g., $\sigma_{\theta} < \sigma_{\varphi}$), but σ_{φ} and σ_{θ} do not correlate. Microlites in flow fronts vary in σ_{φ} from 18° to 50° and σ_{θ} from 14° to 30°. Orientations in near-vent samples have σ_{φ} ranging from 14° to 38° and σ_{θ} ranging from 12° to 31° and are thus as oriented as distal samples (Fig. 7).

Open image in new window

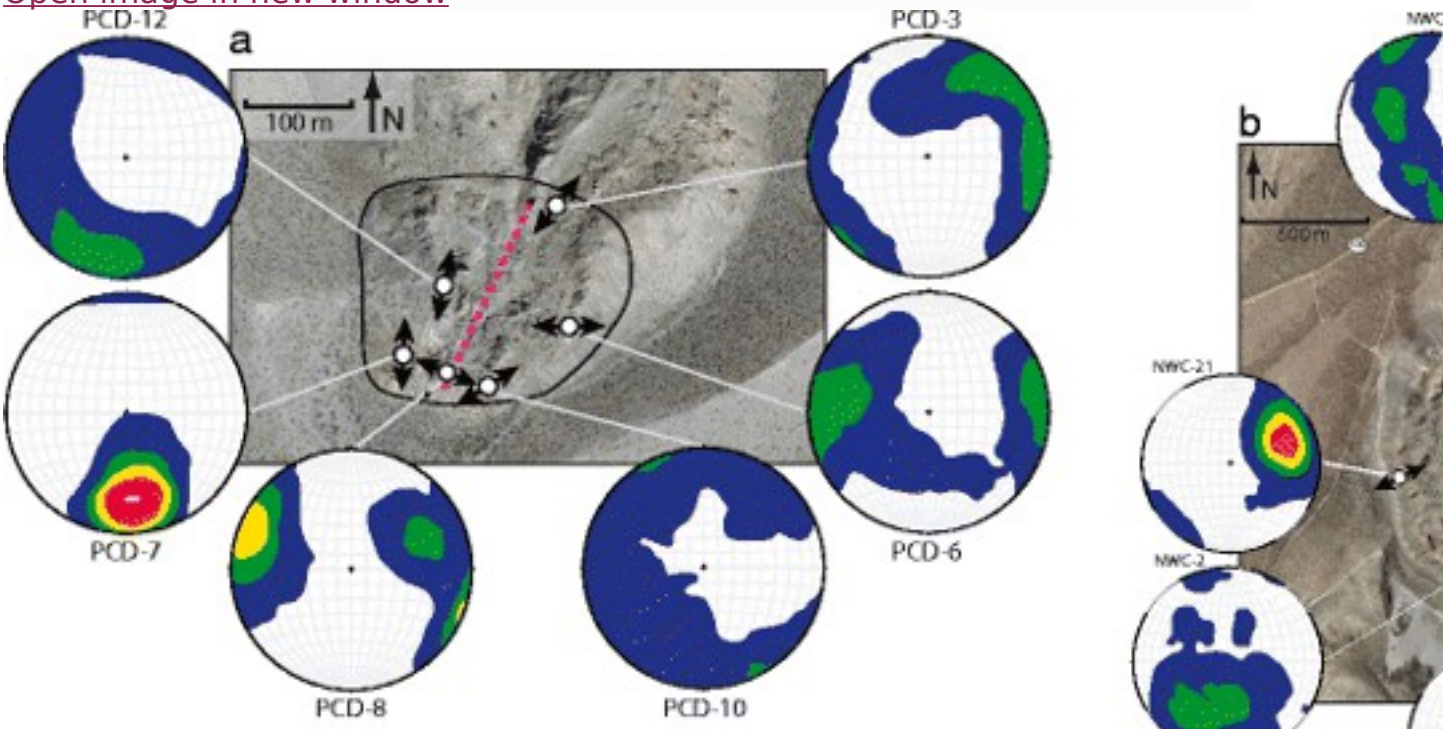

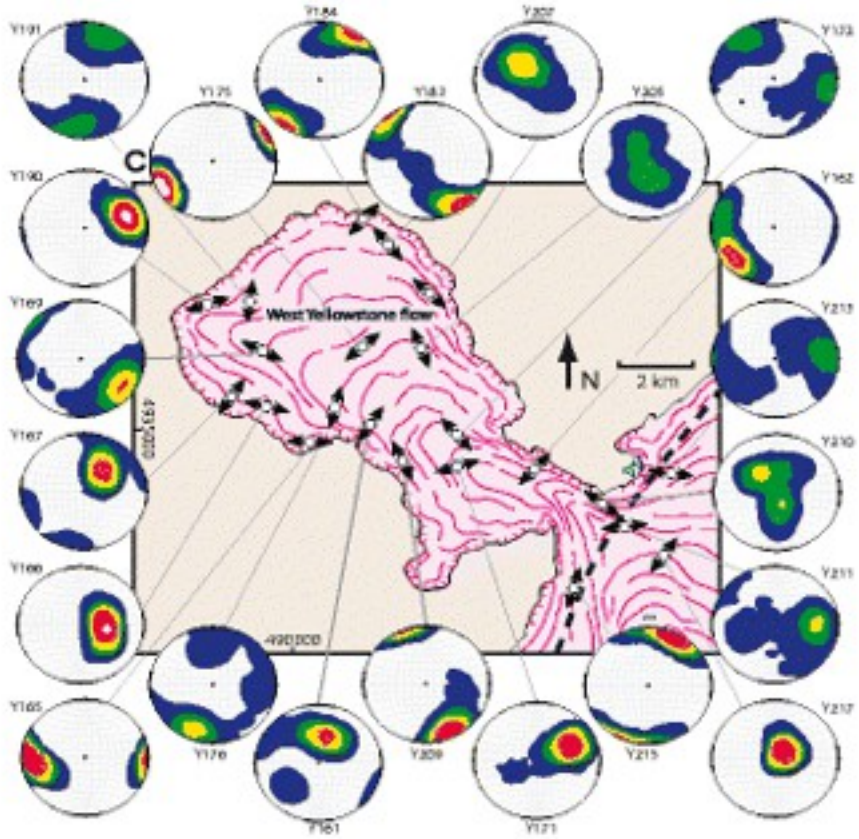

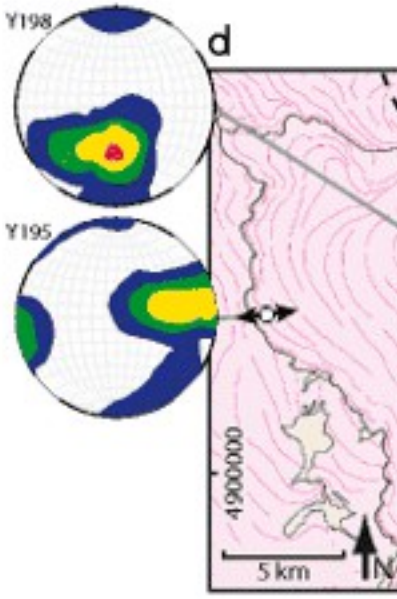

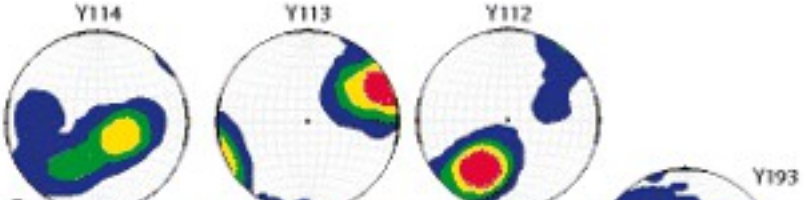

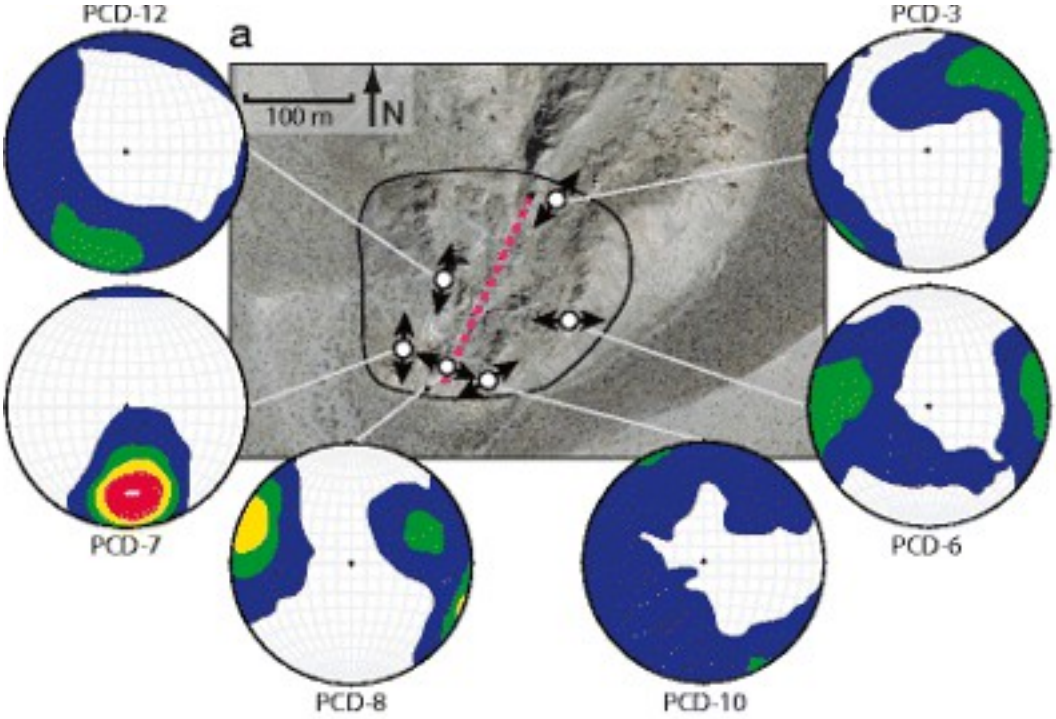
a
PCD-12
PCD-3
100 m
N
PCD-7
PCD-6
PCD-8
PCD-10

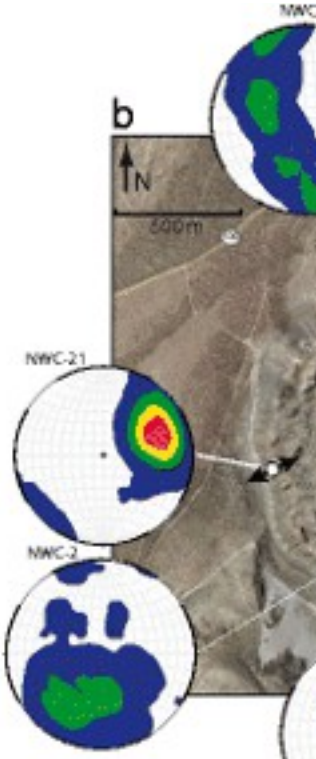
b
N
NWC-21
NWC-2

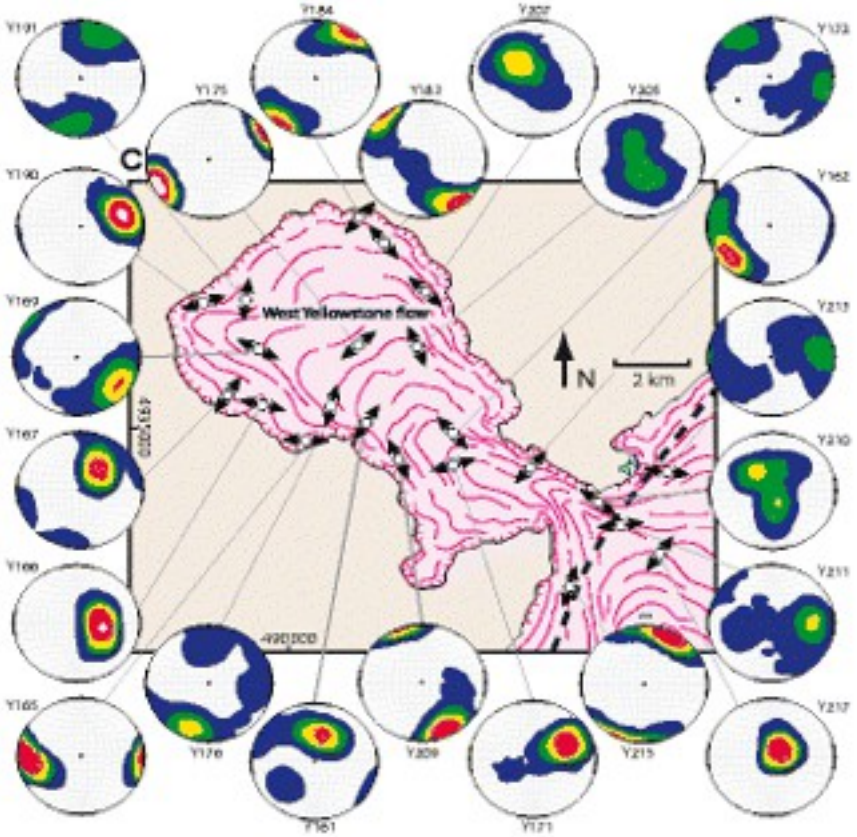
c
West Yellowstone flow
N
2 km

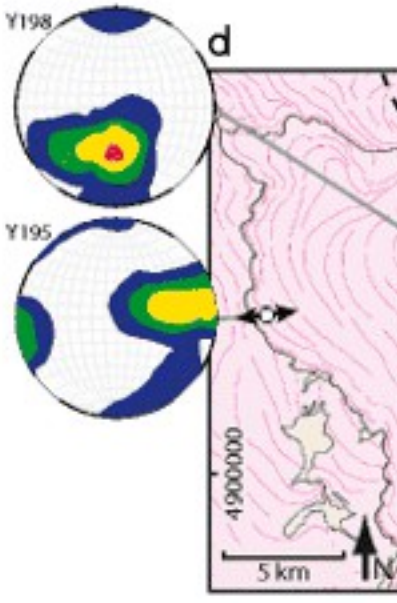
Y198
Y195
d
5 km
N

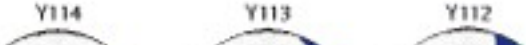
Y114
Y113
Y112

Fig. 6
Stereograms for acicular microlite orientation distributions across the lava flows and domes. The *black arrows* show the dominant microlite trend. The degree of microlite alignment is represented by stereograms with Kamb contours, with *colors* representing orientation frequency per unit area (where *blue* is 2 %, *green* is 8 %, *yellow* is 14 %, *orange* is 20 %, *red* is 26 %, and *pink* is 32 %). **a** South Dome at Panum Crater. The extent of the dome is marked by the *black line*. Trend of central fissure vent is marked by the *dashed line*. **b** Northwest Coulee, **c** the western lobe of West Yellowstone, **d** Summit Lake, and **e** Pitchstone Plateau. Air photos of Mono Craters are from Google Maps. Geologic maps of Central Plateau Member rhyolites (*pink*) are modified after Christiansen (2001). *Dark pink lines* on those flows represent pressure ridges

Open image in new window

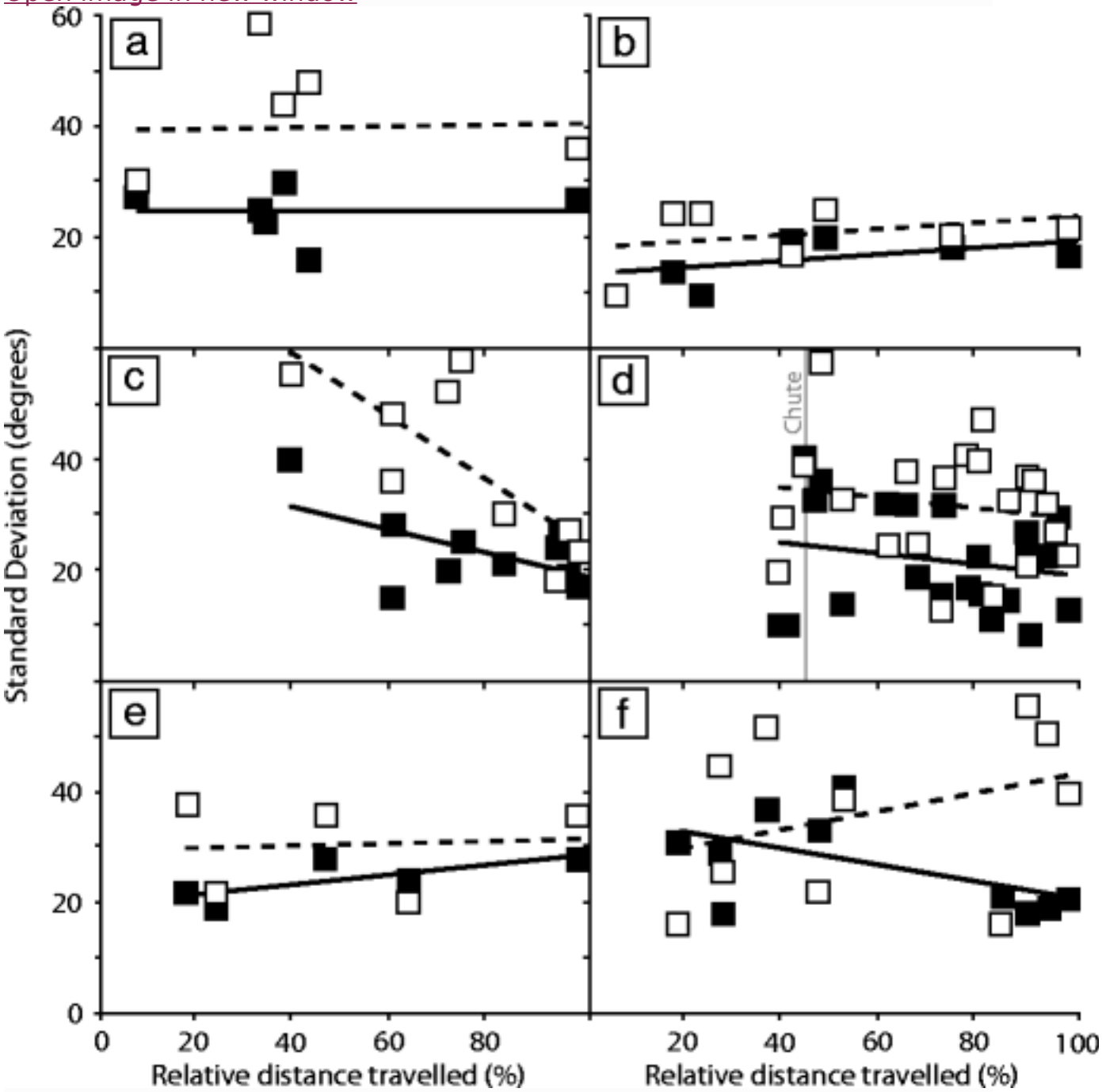

Fig. 7
Standard deviation of microlite orientation as a function of position in **a** South Dome at Panum Crater and **b** Douglas Knob [reproduced from Befus et al. (2014)]. **c** Northwest Coulee, **d** West Yellowstone, **e** Summit Lake, and **f** Pitchstone Plateau. *White squares* are standard deviations of trend, and *black squares* are standard deviations of plunge. The *dashed and solid black lines* are linear regressions through the trend and plunge data,

respectively. Relative distance travelled measurements are percentages of flow distance from vent relative to maximum flow distance

Although South Dome samples were geographically separated from one another by no more than 200 m, microlite orientations range from near random to strongly aligned (Fig. 6a). Standard deviations of trend and plunge vary from 22° to 59° and 16° to 30°, respectively. In addition, microlites generally are nearly horizontal, with plunge distributions better aligned than trend.

The standard deviations of microlite orientations in samples from the large-volume lavas display the same ranges in orientation as South Dome and Douglas Knob lava domes (Figs. 6and 7). Even microlites in distal portions of the extensive Summit Lake and Pitchstone Plateau lava flows are no more aligned than those at their vents. Standard deviation of trend and plunge show no correlation with distance from the vent or eruptive volume. Indeed, small- and large-volume flows show similar degrees of alignment (Fig. 7).

Experimental data

Most crystallization occurs at pressures less than 50 MPa during decompression experiments. At higher final pressures (50 to 100 MPa), some microlite growth is seen, but number densities were too similar to document change. In all experiments, magnetite textures were largely insensitive to temperature, but number density increased slightly with decreasing decompression rate. All decompression experiments at 720 °C crystallized quartz and alkali feldspar (Fig. 8). At the fastest decompression rates, rare quartz and acicular alkali feldspar needles nucleated, whereas experiments at the slowest rates generated coarser intergrowths of alkali feldspar and quartz that comprise ≥20 % of the sample. At 780 °C, new microlite formation of alkali feldspar and clinopyroxene occurred only at 0.4 MPa hr^{-1}, the slowest decompression (Fig. 8). At faster rates, no new crystallization occurred. At 750 °C, both clinopyroxene and alkali feldspar were found to vary with decompression rates (Fig. 8). Rates slower than 2 MPa hr^{-1} led to increased numbers of both alkali feldspar and clinopyroxene, whereas microlite textures were unchanged in faster decompressions. Alkali feldspar occurs as prismatic laths with rare swallowtail terminations, and clinopyroxene occurred as individual crystals or as overgrowths on magnetite crystals.

Open image in new window

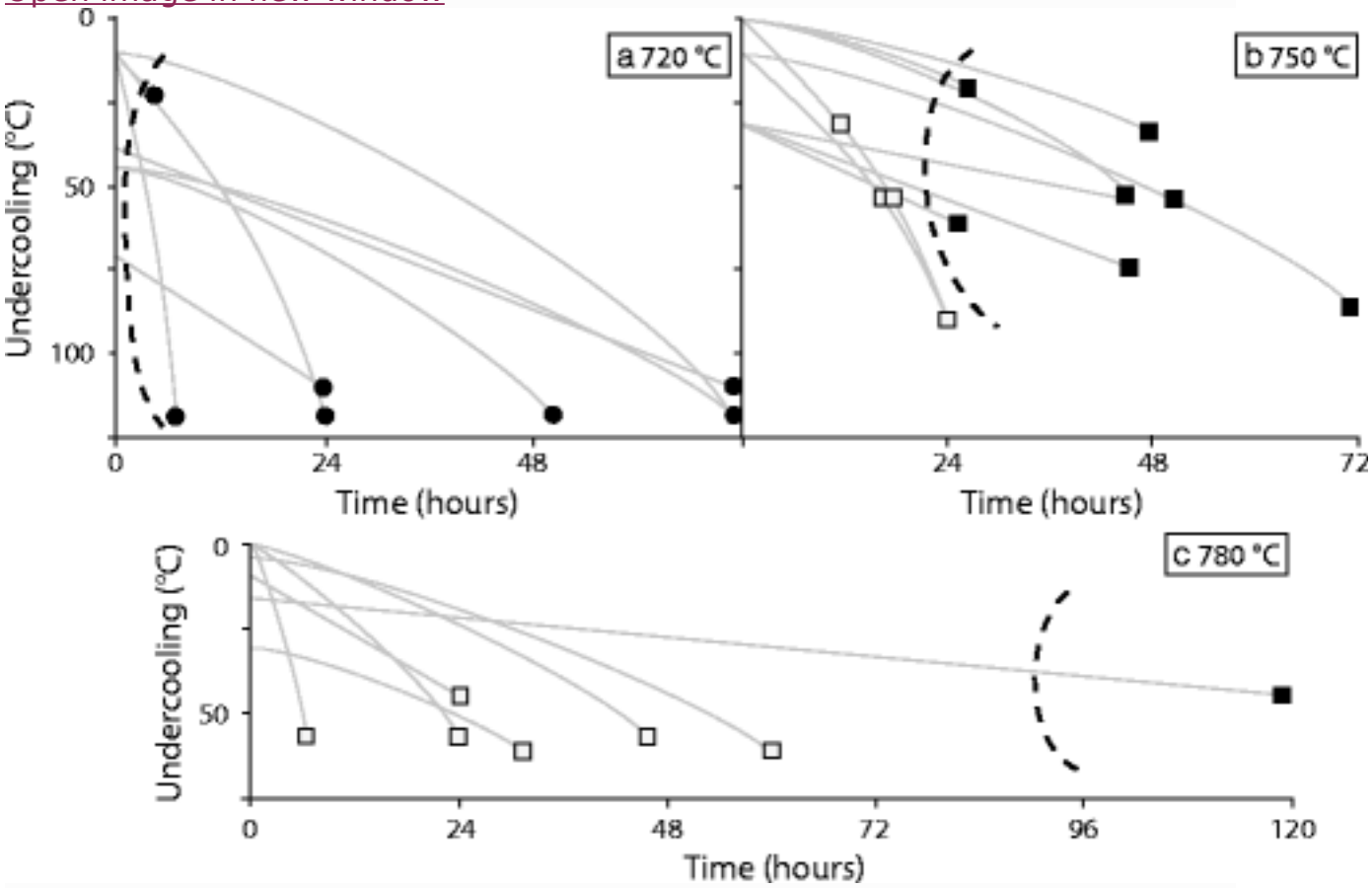

Fig. 8
The relationship between Δ*T* and time for decompression experiments at a 720 °C, b 750 °C, c 780 °C. Decompression pathways are shown with *gray lines* that extend from starting conditions at time zero to final conditions at quench. *Black circles* represent experiments that formed quartz, alkali feldspar, and clinopyroxene; *black squares*represent experiments that formed alkali feldspar and clinopyroxene; and *white squares*show experiments in which no microlites formed. Decompression pathways follow curved and linear trajectories for experiments at NNO + 1 or QFM, respectively, because ΔT are estimated from the sanidine in curve surfaces that were estimated to be curved and linear (Befus 2014). The *dashed lines* separate domains of microlite stability

Discussion

Microlite numbers and orientations in lavas are a cumulative result of conduit flow, degassing, and emplacement. Thus, before they can be used to gain insight into eruption dynamics, it must be deduced when and where orientations and numbers are established during an eruption.

The degree to which acicular microlites align as a whole (i.e., σ_{φ} and σ_{θ} go to smaller values) will increase with increasing strain, which is imparted during emplacement (Manga 1998; Castro et al. 2002). To estimate the shear style and amount of strain that accumulates in lava as it ascends or is emplaced, we compare observed values for microlite σ_{φ} and σ_{θ} to the theoretical response of a population of rods to simple or pure shear flow in three dimensions (Jeffery 1922; Gay 1968; Manga 1998; Befus et al. 2014). Under simple shear, a population of microlites progressively aligns, but individuals continuously rotate, and thus the population never becomes completely aligned. In contrast, microlites can align completely in response to pure shear (standard deviation goes to zero).

The western flow lobe of West Yellowstone lava flow provides an exceptional case to investigate microlite orientation during flow (Fig. 6c). Flow beyond the chute should cause microlite populations to become progressively better aligned. We measured microlite orientations in 17 samples downstream of the chute and in 5 samples in the ponded domain upstream of the chute. Microlite trend and orientations are scattered with respect to distance from the chute and importantly do not become more aligned with increasing distance travelled (Figs. 6c and 7d). The orientation measurements indicate that the microlites did not respond to the bulk flow field during the emplacement of the western lobe of West Yellowstone lava flow.

Similarly, we find that the degree of microlite alignment is insensitive to the relative position in other flows (Fig. 7). Distal samples are statistically indistinguishable from near-vent samples. The standard deviation of microlite orientations from South Dome and Douglas Knob are likewise similar to those measured in the larger flows. In most samples, microlites tend to be oriented closer to horizontal than vertical, but plunge measurements also do not correlate with their position in the flow. No clear relationship exists between microlite trend and our estimates for flow direction, which we infer from the distribution of preserved pressure ridges and position within a flow (e.g., relative to vent and flow fronts).

The degree of alignment of microlites in small domes and larger lavas with high aspect ratios appears to be unaffected by surface emplacement, which implies that preferred orientations are remnants of conduit flow. Indeed, microlites are aligned in near-vent samples. The absence of increased alignment also demonstrates strains accumulated in the sampled portion of the flow during emplacement were small. The lack of progressive alignment can be understood when it is realized that most strain in an actively deforming lava would accumulate mainly near its base (Appendix). The upper surface, where most samples were collected, simply rafts on the deforming lower portions, and hence accumulated little strain (e.g., Befus et al. 2014 show strains less than 2 should cause measureable alignment).

Consequently, microlite orientations from surface samples may indeed preserve orientations inherited from deformation in the conduit.

To establish the timing and location of microlite formation, we first examine MND across large flows that experienced significant spreading. If microlites crystallize during subaerial emplacement, then a progressive increase in number density with distance travelled away from the vent should develop in response to increased undercooling and time. Pitchstone Plateau, Solfatara Plateau, and Summit Lake each travelled more than 10 km, but neither MND for any single phase nor all combined varies across the lengths (Fig. 5). In fact, MND of those extensive flows are identical to those found in small-volume lava domes and near-vent samples where little lateral spreading has occurred. We conclude that microlites were unable to nucleate appreciably during flow along the surface. We suggest that slow chemical diffusion (correlated with elevated viscosity) within the melt prevented microlites from nucleating. Indeed high-silica rhyolite melt at 750 ± 25 °C with ~0.1 wt% dissolved H_2O would have a viscosity of $10^{9–10}$ Pa s (Giordano et al. 2008; Appendix).

Conduit flow and eruption

We have shown that microlite numbers and orientations do not reflect surface transport. Instead, both probably preserve a record of conduit flow. If true, then the diversities of MND and σ_θ and σ_φ across flows reflect spatial and/or temporal variations inherited from the conduit.

Before entering the conduit, phase equilibria experiments, geothermometry, and volatile contents of melt inclusions all indicate that Central Plateau Member rhyolites were stored at 750 ± 25 °C and 50 to 150 MPa in the shallow crust and were in equilibrium with fluid that is 25 to 60 mol% H_2O (Befus 2014). We estimate ΔT of the Yellowstone lavas and our decompression experiments using those phase equilibria constraints (Fig. 2). We have no estimates for the storage conditions of Mono Craters lavas and thus limit our discussion to Yellowstone.

Decompressions at 750 °C formed clinopyroxene and alkali feldspar in decompressions ranging up to 2 MPa hr^{-1} (Fig. 8). Crystal forms and number densities in decompressions ranging from 1–2 MPa hr^{-1} most closely replicate those observed in lavas. Slower rates led to overly abundant alkali feldspar density, which was never seen in natural samples. Faster decompressions did not generate new microlite growth. Decompressions slightly faster than ~2 MPa hr^{-1} may thus be appropriate for lavas that lack feldspar and clinopyroxene (e.g., Buffalo Lake and portions of others).

A decompression rate of ~2 MPa hr^{-1} is equivalent to an ascent rate of ~20–25 mm s^{-1}(~2 km d^{-1}), assuming a lithostatic pressure gradient and a melt density of 2350 kg m^{-3} (Lange and Carmichael 1990). Such slow ascent most likely allowed gas loss from the ascending magma, permitting effusive eruptions (Eichelberger et al. 1986; Jaupart and Allègre 1991; Burgisser and Gardner 2004). Similar slow ascent rates have been estimated for other similar rhyolite lavas and domes emplaced effusively (Rutherford and Gardner 2000; Gonnermann and Manga 2003; Rutherford 2008; Sano et al. 2015), and our estimate is comparable to constraints placed on ascent during the recent effusions at Cordón Caulle and Chaitén (Castro et al. 2013; Pallister et al. 2013). We interpret the variability of MND at the thin section and flow scale to result from waxing and waning ascent rates during pulsatory eruptions and networks of degassing pathways that modify the large-scale degassing process (Gonnermann and Manga 2003; Tuffen et al. 2003, 2008).

The striking resemblance of MND across volumetrically diverse, compositionally similar lavas suggests conduit ascent rates are similar, although thicker and larger volume flows have slightly higher MND, which may indicate slightly faster ascent (Fig. 4). If ascent rates were alike for all flows, then either the conduit dimensions were larger and/or eruptive durations longer for the large-volume flows. We use the lava outline and distribution of surface pressure ridges to trace the path of the flows to their vent sources. The elongate form of lava domes and the distribution of near-vent pressure ridges on flows demonstrate that each lava was likely sourced from a fissure vent (Fig. 1) (Christiansen et al. 2007). We estimate that small-volume lavas were sourced from fissures ranging from 0.5 to 1 km in length, whereas large-volume lavas erupted from fissures 5 to 10 km in length (Fig. 1).

The mean ascent rate U (m s^{-1}) of an incompressible magma during steady, laminar flow between parallel dike walls is

$$U = w^2/12\mu \, dP/dZ \quad (1)$$

where w (m) is the distance between the walls, μ is the melt viscosity (Pa s), and dP/dz is the density contrast between melt and crust multiplied by gravitational acceleration and is assumed to be 1960 Pa m^{-1} (Turcotte and Schubert 1982; Petford et al. 1993). Assuming an average ascent rate is 20 mm s^{-1}, based on our estimate from microlite textures, we can use Eq. 1 to calculate the minimum dike width feeding the eruptions. We calculate a representative range for melt viscosity to be $10^{5.8-7.3}$ Pa s during ascent, assuming a high-silica rhyolitic melt (76 ± 1 wt%) with 2.5 ± 0.5 wt% H_2O, 5 vol% crystallinity, at a temperature of 750 ± 25 °C (Spera 2000; Giordano et al. 2008; Befus 2014). Ascent at 20 mm s^{-1} yields dike widths ranging from 9 to 48 m. The ratio of ascent rate to conduit width provides

strain rates of ~10^{-3} to ~10^{-4} s^{-1}. At such low strain rates, rhyolitic melts are expected to erupt effusively and flow as Newtonian fluids (Webb and Dingwell 1990; Gonnermann and Manga 2003).

Together, our estimates for ascent rate, dike width, and dike length suggest the eruptions that fed the small-volume flows had eruptive fluxes of 90–700 m^3 s^{-1}. Although our calculations have considerable uncertainties, such estimates for the small-volume lavas are similar to an order of magnitude to those witnessed at Chaitén and Cordón Caulle (Pallister et al. 2013; Schipper et al. 2013; Tuffen et al. 2013) and are consistent with estimates for other small-volume lavas (Swanson et al. 1987; Vogel et al. 1989; Nakada and Motomura 1995; Fink and Griffiths 1998; Sparks et al. 1998; Hammer et al. 2000; Rutherford and Gardner 2000; Tuffen et al. 2003; Rutherford 2008; Hautmann et al. 2009; Tuffen and Castro 2009).

Because our estimates are similar to those witnessed for equally small flows, we estimate first-order rates and timescales for large-volume effusive eruptions for which we have no observational constraints (Walker et al. 1973; Bonnichsen and Kauffman 1987; Manley 1996; Pankhurst et al. 2011). Our estimates suggest that the large-volume flows had eruptive fluxes of 1000–6500 m^3 s^{-1}, and the eruptions lasted months to years.

Conduit dynamics

The lavas extruding at their vents have all undergone significant shear, as witnessed by the commonly strong alignment of microlites in vent and near-vent samples (Fig. 7). If we assume alignment was induced by pure shear, then σ_φ indicates that melts experienced strains less than 1.7 (see Manga 1998 and Befus et al. 2014 for details on technique). If instead the melts were deformed by simple shear, then strains reached up to 5.8. Plunge distributions are generally better aligned than trend, and implied strains of 0.7 to 4.2 for pure shear, and 1.2 to “infinite” for simple shear. “Infinite” strain, which occurs in 30 % of the samples, results from the impossibility that simple shear can generate such good alignment. It is thus more likely that pure shear is the dominant mode of deformation. Indeed, given the ascent distances (>1000 m) over which shear would operate during conduit flow after microlites nucleate, it is unlikely that most samples would preserve such small strains if simple shear predominated.

Interestingly, most microlite plunges are aligned closer to horizontal than vertical (Fig. 7). One way such orientations may result would be from gravitational collapse of permeable magma foam in the conduit as it ascends (Eichelberger et al. 1986). Foams form during ascent in the conduit as bubbles nucleate and grow in response to decompression-induced degassing. When porosity reaches a critical threshold, the foam becomes

permeable and gas can escape, which allows stress from the overburden to collapse the foam, depending on melt viscosity (Eichelberger et al. 1986). Expansion and subsequent collapse would strain the magma and thus orient microlites. Specifically, the long axes of microlites should align in the direction of local extension. The observed close to horizontal microlite orientations argues for flattening caused by vertical collapse.

If we allow the melt to deform to its fullest extent, and collapse occurs when porosity reaches 65–75 % (Sparks 1978; Gardner et al. 1996; Namiki and Manga 2008), then a single volumetric collapse event to dense obsidian would generate a strain of 2.4 (e.g., strain = change in length/initial length), similar to strain estimates from microlite orientations. On the other hand, if foam collapses at lower porosities of ~40 % (Klug and Cashman 1996; Saar and Manga 1999; Burgisser and Gardner 2004; Takeuchi et al. 2005), the strain is 0.7, the lowest strain estimated from microlite orientations. Multiple collapses would thus be needed to generate the full range of strains.

Conclusion

We characterized microlite textures in a range of rhyolite lavas to investigate their eruption dynamics. We conclude that microlite orientations and number densities did not evolve during surface flow. Instead, those textures are relics of conduit flow and can thus be used to infer conduit dynamics. Because microlite textures across small- and large-volume eruptions are so similar, we suggest that slow conduit ascent rates operate irrespective of eruptive volume. Natural microlite assemblages and number densities are most comparable to those generated during experimental decompressions at 1 to 2 MPa hr^{-1} and 750 °C. Flows lacking clinopyroxene and alkali feldspar may have decompressed at slightly faster rates. Small-volume eruptions experienced small eruptive fluxes and were active for weeks to months, whereas the large-volume lavas had high fluxes and remained active for months to years. In most samples, microlite plunge is better aligned than trend, which requires strains to be imparted by pure shear, and may reflect collapse of permeable foam in the conduit.

Notes

Acknowledgments

The authors thank Ben Andrews, Kevin Befus, Ryan Cahalan, Joey Cleveland, Brent Jackson, Jake Jordan, Tim Prather, Noah Randolph-Flagg, and Robert Zinke for their help in the field. This research was made possible by grants from the National Science Foundation to J.E.G. (EAR-1049829), M.M (EAR-1049662 and NSF SEES), and a National Park Service research permit (YELL-05678).

Supplementary material

445_2015_971_MOESM1_ESM.pdf (787 kb)
ESM 1 (PDF 786 kb)

References

1. Bacon CR, Hirschmann MM (1988) Mg/Mn partitioning as a test for equilibrium between coexisting Fe-Ti oxides. Am Mineral 73:57–61Google Scholar

2. Befus KS (2014) Storage, ascent, and emplacement of rhyolite lavas. Dissertation, University of Texas at AustinGoogle Scholar

3. Befus KS, Zinke RW, Jordan JS et al (2014) Pre-eruptive storage conditions and eruption dynamics of a small rhyolite dome: Douglas Knob, Yellowstone volcanic field, USA. Bull Volcanol 76:1–12. doi: 10.1007/s00445-014-0808-8CrossRefGoogle Scholar

4. Bonnichsen B, Kauffman DF (1987) Physical features of rhyolite lava flows in the snake river plain volcanic province, southwestern Idaho. In: Fink JH (ed) The emplacement of silicic domes and lava flows. Geol Soc Am Spec Pap 212:118–145Google Scholar

5. Burgisser A, Gardner JE (2004) Experimental constraints on degassing and permeability in volcanic conduit flow. Bull Volcanol 67:42–56. doi: 10.1007/s00445-004-0359-5CrossRefGoogle Scholar

6. Cañón-Tapia E, Castro J (2004) AMS measurements on obsidian from the Inyo Domes, CA: a comparison of magnetic and mineral preferred orientation fabrics. J Volcanol Geotherm Res 134:169–182. doi: 10.1016/j.jvolgeores.2004.01.005CrossRefGoogle Scholar

7. Cardozo N, Allmendinger RW (2013) Spherical projections with OSXStereonet. Comput Geosci 51:193–205. doi: 10.1016/j.cageo.2012.07.021CrossRefGoogle Scholar

8. Carroll MR, Blank JG (1997) The solubility of H2O in phonolitic melts. Am Mineral 82:549–556Google Scholar

9. Castro J, Manga M, Cashman K (2002) Dynamics of obsidian flows inferred from microstructures: insights from microlite preferred orientations. Earth Planet Sci Lett 199:211–226. doi: 10.1016/S0012-821X(02)00559-9CrossRefGoogle Scholar

10. Castro J, Cashman KV, Manga M (2003) A technique for measuring 3D crystal-size distribution of prismatic microlites in obsidian. Am Mineral 88:1230–1240CrossRefGoogle Scholar

11. Castro JM, Schipper CI, Mueller SP et al (2013) Storage and eruption of near-liquidus rhyolite magma at Cordón Caulle, Chile. Bull Volcanol 75:1–17. doi: 10.1007/s00445-013-0702-9CrossRefGoogle Scholar

12. Christiansen RL (2001) The Quaternary and Pliocene Yellowstone Plateau volcanic field of Wyoming, Idaho, and Montana. USGS Professional Paper 729-G, 120 pGoogle Scholar

13. Christiansen RL, Lowenstern JB, Smith RB, Heasler H, Morgan LA, Nathenson M, Mastin LG, Muffler LJP, Robinson JE (2007) Preliminary assessment of volcanic and hydrothermal hazards in Yellowstone National Park and vicinity. USGS Open-file report 2007–1071, 98 pGoogle Scholar

14. Davis BK, McPhie J (1996) Spherulites, quench fractures and relict perlite in a Late Devonian rhyolite dyke, Queensland, Australia. J Volcanol Geotherm Res 71:1–11. doi: 10.1016/0377-0273(95)00063-1CrossRefGoogle Scholar

15. Eichelberger JC, Carrigan CR, Westrich HR, Price RH (1986) Non-explosive silicic volcanism. Nature 323:598–602. doi: 10.1038/323598a0CrossRefGoogle Scholar

16. Fink J (1980) Surface folding and viscosity of rhyolite flows. Geology 8:250–254. doi: 10.1130/0091-7613(1980)8<250:SFAVOR>2.0.CO;2CrossRefGoogle Scholar

17. Fink JH, Griffiths RW (1998) Morphology, eruption rates, and rheology of lava domes: insights from laboratory models. J Geophys Res Solid Earth 103:527–545. doi: 10.1029/97JB02838CrossRefGoogle Scholar

18. Gardner JE, Thomas RME, Jaupart C, Tait S (1996) Fragmentation of magma during Plinian volcanic eruptions. Bull Volcanol 58:144–162. doi: 10.1007/s004450050132CrossRefGoogle Scholar

19. Gay NC (1968) The motion of rigid particles embedded in a viscous fluid during pure shear deformation of the fluid. Tectonophysics 5:81–88CrossRefGoogle Scholar

20. Giordano D, Russell JK, Dingwell DB (2008) Viscosity of magmatic liquids: a model. Earth Planet Sci Lett 271:123–134. doi: 10.1016/j.epsl.2008.03.038CrossRefGoogle Scholar

21. Gonnermann HM, Manga M (2003) Explosive volcanism may not be an inevitable consequence of magma fragmentation. Nature 426:432–435. doi: 10.1038/nature02138CrossRefGoogle Scholar

22. Gregg TKP, Fink JH, Griffiths RW (1998) Formation of multiple fold generations on lava flow surfaces: influence of strain rate, cooling rate, and lava composition. J Volcanol Geotherm Res 80:281–292. doi: 10.1016/S0377-0273(97)00048-6CrossRefGoogle Scholar

23. Hammer JE, Cashman KV, Voight B (2000) Magmatic processes revealed by textural and compositional trends in Merapi dome lavas. J Volcanol Geotherm Res 100:165–192CrossRefGoogle Scholar

24. Harker A, (1897) Petrology for students, Cambridge, 334 pGoogle Scholar

25. Hautmann S, Gottsmann J, Sparks RSJ et al (2009) Modeling ground deformation caused by oscillating overpressure in a dyke conduit at Soufrière Hills Volcano, Montserrat. Tectonophysics 471:87–95. doi: 10.1016/j.tecto.2008.10.021CrossRefGoogle Scholar

26. Hildreth W (2004) Volcanological perspectives on Long Valley, Mammoth Mountain, and Mono Craters: several contiguous but discrete systems. J Volcanol Geotherm Res 136:169–198CrossRefGoogle Scholar

27. Iezzi G, Ventura G (2000) Kinematics of lava flows based on fold analysis. Geophys Res Lett 27:1227–1230. doi: 10.1029/1999GL011279CrossRefGoogle Scholar

28. Jaupart C, Allègre CJ (1991) Gas content, eruption rate and instabilities of eruption regime in silicic volcanoes. Earth Planet Sci Lett 102:413–429. doi: 10.1016/0012-821X(91)90032-DCrossRefGoogle Scholar

29. Jeffery GB (1922) The motion of ellipsoidal particles immersed in a viscous fluid. Proc Roy Soc Lond 102:161–179CrossRefGoogle Scholar

30. Kelleher PC, Cameron KL (1990) The geochemistry of the Mono Craters-Mono Lake islands volcanic complex, Eastern California. J Geophys Res 95:17643–17659CrossRefGoogle Scholar

31. Klug C, Cashman KV (1996) Permeability development in vesiculating magmas: implications for fragmentation. Bull Volcanol 58:87–100. doi: 10.1007/s004450050128CrossRefGoogle Scholar

32. Lange RL, Carmichael ISE (1990) Thermodynamic properties of silicate liquids with emphasis on density, thermal expansion and compressibility. Rev Mineral Geochem 24:25–64Google Scholar

33. Lofgren G (1974) An experimental study of plagioclase crystal morphology: isothermal crystallization. Am J Sci 274:243–273CrossRefGoogle Scholar

34. Manga M (1998) Orientation distribution of microlites in obsidian. J Volcanol Geotherm Res 86:107–115. doi: 10.1016/S0377-0273(98)00084-5CrossRefGoogle Scholar

35. Manley CR (1996) Physical volcanology of a voluminous rhyolite lava flow: the Badlands lava, Owyhee Plateau, southwestern Idaho. J Volcanol Geotherm Res 71:129–153. doi: 10.1016/0377-0273(95)00066-6CrossRefGoogle Scholar

36. Miller DC (1985) Holocene eruptions at the Inyo volcanic chain, California: implications for possible eruptions in Long Valley caldera. Geology 13:14–17CrossRefGoogle Scholar

37. Nakada S, Motomura Y (1995) Manner of magma ascent at Unzen Volcano (Japan). Geophys Res Lett 22:567–570CrossRefGoogle Scholar

38. Namiki A, Manga M (2008) Transition between fragmentation and permeable outgassing of low viscosity magmas. J Volcanol Geotherm Res 169:48–60CrossRefGoogle Scholar

39. Nowak M, Cichy SB, Botcharnikov RE et al (2011) A new type of high-pressure low-flow metering valve for continuous decompression: first experimental results on degassing of rhyodacitic melts. Am Mineral 96:1373–1380. doi: 10.2138/am.2011.3786CrossRefGoogle Scholar

40. Pallister JS, Diefenbach AK, Burton WC et al (2013) The Chaitén rhyolite lava dome: eruption sequence, lava dome volumes, rapid effusion rates and source of the rhyolite magma. Andean Geol. doi: 10.5027/andgeoV40n2-a06Google Scholar

41. Pankhurst MJ, Schaefer BF, Betts PG et al (2011) A Mesoproterozoic continental flood rhyolite province, the Gawler Ranges, Australia: the end member example of the Large Igneous Province clan. Solid Earth 2:25–33. doi: 10.5194/se-2-25-2011CrossRefGoogle Scholar

42. Petford N, Kerr RC, Lister JR (1993) Dike transport of granitoid magmas. Geology 21:845–848CrossRefGoogle Scholar

43. Rust AC, Manga M, Cashman KV (2003) Determining flow type, shear rate and shear stress in magmas from bubble shapes and orientations. J Volcanol Geotherm Res 122:111–132. doi: 10.1016/S0377-0273(02)00487-0CrossRefGoogle Scholar

44. Rutherford MJ (2008) Magma ascent rates. Rev Mineral Geochem 69:241–271CrossRefGoogle Scholar

45. Rutherford MJ, Gardner JE (2000) Rates of magma ascent. In: Sigurdsson H (ed) Encyclopedia of volcanoes. Academic, New York, pp 207–217Google Scholar

46. Saar MO, Manga M (1999) Permeability-porosity relationship in vesicular basalts. Geophys Res Lett 26:111–114. doi: 10.1029/1998GL900256CrossRefGoogle Scholar

47. Sano K, Wada K, Sato E (2015) Rates of water exsolution and magma ascent inferred from microstructures and chemical analyses of the Tokachi-Ishizawa obsidian lava, Shirataki, northern Hokkaido, Japan. J Volcanol Geotherm Res 292:29–40CrossRefGoogle Scholar

48. Schipper CI, Castro JM, Tuffen H et al (2013) Shallow vent architecture during hybrid explosive–effusive activity at Cordón Caulle (Chile, 2011–12): evidence from direct observations and pyroclast textures. J Volcanol Geotherm Res 262:25–37. doi: 10.1016/j.jvolgeores.2013.06.005CrossRefGoogle Scholar

49. Sieh K, Bursik M (1986) Most recent eruption of the Mono Craters, eastern central California. J Geophys Res Solid Earth 91:12539–12571. doi: 10.1029/JB091iB12p12539CrossRefGoogle Scholar

50. Smith JV (2002) Structural analysis of flow-related textures in lavas. Earth-Sci Rev 57:279–297. doi: 10.1016/S0012-8252(01)00081-2CrossRefGoogle Scholar

51. Sparks RSJ (1978) The dynamics of bubble formation and growth in magmas: a review and analysis. J Volcanol Geotherm Res 3:1–37. doi: 10.1016/0377-0273(78)90002-1CrossRefGoogle Scholar

52. Sparks RSJ, Young SR, Barclay J, Calder ES, Cole P, Darroux B, Davies MA, Druitt TH, Harford C, Herd R, James M, Lejeune AM, Loughlin S, Norton G, Skerrit G, Stasiuk MV, Stevens NS, Toothill J, Wadge G, Watts R (1998) Magma production and growth of the lava dome of the Soufriere Hills Volcano, Montserrat, West Indies: November 1995 to December 1997. Geophys Res Lett 25:3421–3424CrossRefGoogle Scholar

53. Stevenson RJ, Hodder APW, Briggs RM (1994) Rheological estimates of rhyolite lava flows from the Okataina Volcanic Centre, New Zealand. N Z J Geol Geophys 37:211–221. doi: 10.1080/00288306.1994.9514616CrossRefGoogle Scholar

54. Swanson DA, Dzurisin D, Holcomb RT, Iwatsubo EY, Chadwick WW, Casadevall TJ, Ewert JW, Heliker CC (1987) Growth of the lava dome at Mount St. Helens, Washington, (USA), 1981–1983. Geol Soc Am Spec Paper 212:1–16CrossRefGoogle Scholar

55. Takeuchi S, Nakashima S, Tomiya A, Shinohara H (2005) Experimental constraints on the low gas permeability of vesicular magma during decompression. Geophys Res Lett 32:n/a–n/a. doi: 10.1029/2005GL022491

56. Tuffen H, Castro JM (2009) The emplacement of an obsidian dyke through thin ice: Hrafntinnuhryggur, Krafla Iceland. J Volcanol Geotherm Res 185:352–366CrossRefGoogle Scholar

57. Tuffen H, Dingwell DB, Pinkerton H (2003) Repeated fracture and healing of silicic magma generate flow banding and earthquakes? Geology 31:1089–1092. doi: 10.1130/G19777.1CrossRefGoogle Scholar

58. Tuffen H, Smith R, Sammonds PR (2008) Evidence for seismogenic fracture of silicic magma. Nature 453:511–514. doi: 10.1038/nature06989CrossRefGoogle Scholar

59. Tuffen H, James MR, Castro JM, Schipper CI (2013) Exceptional mobility of an advancing rhyolitic obsidian flow at Cordon Caulle volcano in Chile. Nat Commun 4:2709. doi: 10.1038/ncomms3709CrossRefGoogle Scholar

60. Turcotte DL, Schubert G (1982) Geodynamics, New York, pp 1–450Google Scholar

61. Vogel TA, Eichelberger JC, Younker LW et al (1989) Petrology and emplacement dynamics of intrusive and extrusive rhyolites of Obsidian Dome, Inyo Craters Volcanic Chain, eastern California. J Geophys Res Solid Earth 94:17937–17956. doi: 10.1029/JB094iB12p17937CrossRefGoogle Scholar

62. Walker GPL, Huntingdon AT, Sanders AT, Dinsdale JL (1973) Lengths of lava flows [and discussion]. Philos Trans R Soc Lond Ser Math Phys Sci 274:107–118. doi: 10.1098/rsta.1973.0030CrossRefGoogle Scholar

63. Webb SL, Dingwell DB (1990) The onset of non-Newtonian rheology of silicate melts. Phys Chem Miner 17:125–132. doi: 10.1007/BF00199663CrossRefGoogle Scholar

64. Williams M, Befus KS, Gardner JE (2012) Magmatic storage conditions along the Mono Craters chain, Eastern California. Amer Geophy Union FM, C2848Google Scholar

65. Wood SH (1983) Chronology of late pleistocene and holocene volcanics, long valley and mono basin geothermal areas, eastern California, technical report. US Geol Surv Open File Rep 83:1–76Google Scholar